UNIVERSIDADE FEDERAL DO RIO GRANDE DO SUL
INSTITUTO DE MATEMÁTICA
PROGRAMA DE PÓS-GRADUAÇÃO EM MATEMÁTICA APLICADA

Nyström Method Applied to Two-dimensional Neutral Particle Transport Problems in Heterogeneous Media

por

Gustavo Alcides Lorensi

Trabalho submetido como requisito parcial
para a obtenção do título de

Doutor em Matemática Aplicada

Prof. Dr. Fabio Souto De Azevedo
Orientador

Prof. Dr. Esequia Sauter
Co-Orientador

Prof. Dr. Richard Vasques
Co-Orientador do Exterior

Porto Alegre, maio de 2024.

CIP - CATALOGAÇÃO NA PUBLICAÇÃO

Alcides Lorensi, Gustavo

Nyström Method Applied to Two-dimensional Neutral Particle Transport Problems in Heterogeneous Media / Gustavo Alcides Lorensi.—Porto Alegre: PPGMAp da UFRGS, 2024.

90 p.: il.

Tese (Doutorado) —Universidade Federal do Rio Grande do Sul, Programa de Pós-Graduação em Matemática Aplicada, Porto Alegre, 2024.
Orientador: De Azevedo, Fabio Souto; Co-Orientador: Sauter, Esequia; Co-Orientador do Exterior: Vasques, Richard

Tese: Matemática Aplicada,
Matemática Aplicada, Teoria de Transporte de Partículas, Método de Nyström

Nyström Method Applied to Two-dimensional Neutral Particle Transport Problems in Heterogeneous Media

por

Gustavo Alcides Lorensi

Trabalho submetido ao Programa de Pós-Graduação em Matemática Aplicada do Instituto de Matemática da Universidade Federal do Rio Grande do Sul, como requisito parcial para a obtenção do título de

Doutor em Matemática Aplicada

Linha de Pesquisa: Teoria de Transporte de Partículas

Orientador: Prof. Dr. Fabio Souto De Azevedo

Co-Orientador: Prof. Dr. Esequia Sauter

Co-Orientador do Exterior: Prof. Dr. Richard Vasques

Banca examinadora:

Prof. Dr. Cássio Baissvenger Pazinatto
IFSul

Prof. Dra. Cibele Aparecida Ladeia
PPGMAp-UFRGS

Prof. Dr. Roberto David Martinez Garcia
IEAv-DCTA

Prof. Dr. Rubem Mário Figueiró Vargas
PUCRS

Tese defendida em
31 de Maio de 2024.

Prof. Dr. Lucas da Silva Oliveira
Coordenador

ACKNOWLEDGEMENTS

I am immensely grateful to everyone who contributed to the success of this research.

My deepest appreciation to my advisors, Prof. Dr. Fabio S. de Azevedo and Prof. Dr. Esequia Sauter. Their profound expertise and understanding were essential in guiding my research. The support, lectures, recommendations, and faith in my abilities have been inspirational throughout this journey.

I am also immensely thankful to my educators, peers, and friends. A special thank you to my colleague and friend, César, who motivated me to embark on this academic journey and supported me throughout all these years.

I want to express my deepest gratitude to Prof. Dr. Richard Vasques, who accepted me into the exchange program. Your vast experience and knowledge were invaluable to me. The lessons I learned under your guidance have profoundly shaped my academic and personal growth. Let's Go Bucks!

The exchange also introduced me to remarkable individuals like Leonardo and Sunday. Their friendship and support during challenging times were invaluable, enriching my experience both educationally and personally.

I am forever grateful to my parents for their constant support and for shaping my ethical and moral foundations, which have been crucial to my growth.

The Graduate Program in Applied Mathematics (PPGMAp) for the opportunity.

The CAPES and CNPq, for their financial support.

SUMMARY

LIST OF FIGURES

LIST OF TABLES

LIST OF ACRONYMS AND SYMBOLS

List of Acronyms

ADO	Analytical Discrete Ordinates
$AHOT$	Arbitrarily High Order Transport
DD	Diamond Difference
F_N	Facile method
GSL	GNU Scientific Library
LN	Linear Nodal
LTS_N	Laplace Transform S_N
P_N	Spherical harmonics
S_N	Discrete ordinates
SGF	Spectral Green's Function
SK_N	Synthetic kernel
SP_N	Simplified P_N

List of Symbols

a, b	Domain length (cm)
a_s, b_s	Source length (cm)
D	Domain, $D = [0, a] \times [0, b]$
E	Particle energy (MeV)

Ki_1	Bickley-Naylor function of the first kind
Ki_2	Bickley-Naylor function of the second kind
n	Expected number of particles (neutrons.cm^{-3})
$\mathbf{n}$	Unit normal (to surface) vector
N_R	Number of subregions/subregions
S	Internal source (cm^{-3}s^{-1})
R_i	Region i
t	Time (s)
v	Particle speed (cm.s^{-1})
$\mathbf{x}, \mathbf{y}$	Position variables
∂D	Boundary of D
λ_c	Dominant eigenvalue
Δ	Variable related to the number of points in a subregion
η	Cosine of the elevation angle
σ_t	Total macroscopic cross section (cm^{-1})
σ_{tR}	Total macroscopic cross section of region R (cm^{-1})
σ_s	Scattering macroscopic cross section (cm^{-1})
σ_{sR}	Scattering macroscopic cross section of region R (cm^{-1})
σ_c	Inverse of the largest eigenvalue of the operator L_g
Φ	Scalar flux (neutrons.cm^{-2}s^{-1})

Ψ	Angular flux (neutrons.cm^{-2}s^{-1}sr^{-1})
Ω	Angular unit vector
∇	Gradient operator

ABSTRACT

The transport equation has a wide range of applications, including neutron transport and heat transfer, among others. Due to its high number of dimensions in the phase space and its integro-differential structure, the numerical simulation of this equation tends to be difficult and with high computational complexity, necessitating efficient and low-cost computational methods. This dissertation advances the field by applying the Nyström method, combined with a singularity-subtraction technique, to two-dimensional fixed-source neutron transport problems. Unlike previous studies, this work introduces novel analytical and computational strategies, including domain subregioning, the clipping distance technique, and the manipulation of the Bickley-Naylor function. Such techniques play a crucial role in optimizing computational processes by identifying and eliminating redundant or non-essential calculations, increasing accuracy and efficiency. The methodology demonstrates significant improvements in solving two-dimensional homogeneous and heterogeneous medium problems with isotropic scattering. By addressing several benchmark problems and showing the method's potential for broader applications, this research contributes a valuable computational tool to transport theory, offering perspectives for dealing with more complex scenarios in the future.

RESUMO

A equação de transporte apresenta uma ampla gama de aplicações, incluindo o transporte de nêutrons e a transferência de calor, entre outras. Devido ao seu elevado número de dimensões no espaço de fase e à sua estrutura integro-diferencial, simulações numéricas desta equação tendem a ser difíceis e com alta complexidade computacional, necessitando métodos computacionais eficientes e de baixo custo computacional. Esta tese avança no campo aplicando o método de Nyström, combinado com a técnica de subtração de singularidade, em problemas de transporte de nêutrons bidimensionais com fonte fixa. Diferentemente de estudos anteriores, este trabalho introduz estratégias analíticas e computacionais inovadoras, incluindo a subdivisão do domínio, a *Clipping Technique* e a manipulação e simplificação da função de Bickley-Naylor. Tais técnicas desempenham um papel crucial na otimização dos processos computacionais ao identificar e eliminar cálculos redundantes ou não essenciais, aumentando a precisão e a eficiência computacional. A metodologia demonstra melhorias significativas na resolução de problemas em meios homogêneos e heterogêneos bidimensionais com espalhamento isotrópico. Ao abordar vários problemas de referência e mostrar o potencial do método para aplicações mais amplas, esta pesquisa contribui com uma ferramenta computacional valiosa para a teoria do transporte, oferecendo perspectivas para lidar com cenários mais complexos no futuro.

1 INTRODUCTION

Formulated initially for the study of the kinetic theory of gases in 1872 by Ludwig Boltzmann [28], the transport equation has been used in a wide range of applications over the years. Some of them are neutron transport [63], heat transfer [77], radiation in gas turbines [31], astronomy [76], fluorescence tomography [47] and photon and electron radiotherapy [81]. Therefore, due to its importance and wide applicability, the search for accurate and quick results has been the focus of interest of many research groups.

As highlighted by Duderstand and Martin in their work [48], several mathematical methodologies have been employed in an effort to derive analytical solutions for transport phenomena across diverse geometrical settings. However, the inherent complexity and specificity of real-world engineering challenges often surpass the applicability of such analytical solutions due to their reliance on overly simplified configurations [70]. Thus, this complexity has led the research community to pivot towards the adoption of numerical methods. These computational techniques have opened new avenues for addressing and solving complex problems that were previously deemed intractable through analytical approaches [70]. More recently, as a way of increasing accuracy and performance, hybrid techniques that mix mathematical and numerical treatments have been applied.

The difficulty in solving the neutron transport equation is due, in part, to the high number of variables in the phase space and to its integro-differential structure [8, 16, 24, 70]. Although the advancement of technology allows faster and more robust computers to be produced, alone this is not enough to solve more realistic problems. It requires a mix of analytical and numerical techniques, along with the use of computational tools and software, to fully address and analyze the variety of issues we encounter. This combination ensures we can tackle both the theoretical aspects and the practical complexities of real-world problems effectively.

Therefore, several numerical methods have been developed by different authors and research groups with the aim of solving this difficulty. Lists of these methods are presented in [1, 10, 16, 48].

The modeling of the process of neutron transport generally follows two different approaches: the probabilistic approach or the deterministic approach [31, 70]. Among the probabilistic methods, which, their name refers, seek to solve transport problems from a more probabilistic point of view, for instance, Monte Carlo methods [36, 77, 95].

Among the deterministic methods, is the discrete ordinates method (S_N) [1, 32, 70], which consists in discretizing the angular variable and solving a system of ordinary differential equations. This classic approach has been generalized and improved, as described by Barichello and Siewert [22] and Abreu [41]. In addition, it is a method that has already been consolidated among researchers and has produced results with high precision and efficiency. Still, in the deterministic methods, stand out the nodal methods [18,23,67], integral methods [3,10,13,72,90], SP_N [64], LTS_N [57,87], and F_N methods [52,56,93], each with their own particularities.

It should be noted that the discrete ordinates or discrete-ordinates-like methods display computational anomalies, called "ray effects", originating from the discretization of the angular variables [10, 33, 65]. On the other hand, the integral methods are known for mitigating ray effects and producing more precise numerical results [11,88]. This is due to the fact that discrete-ordinates-like methods are based on expanding the integral of the transport equation in discrete directions, "rays", while integral methods are based on using the integral formulation of the transport equation. This way, there is no need to discretize the angular variable, but rather to calculate the integral numerically. However, they may produce complex algorithms with an elevated computational cost [89].

Integral methods have been shown to be effective in treating transport problems in Cartesian and Cylindrical geometry [6, 13, 29, 30, 89]. However, when compared to other deterministic methods, the number of research works related to particle transport is still scarce and the literature contains only a limited number of works with high-precision results.

As mentioned earlier, transport problems were explored using a variety of methods. Regarding one-dimensional (1-D) problems, high precision benchmarks for problems in a homogeneous slab case were obtained with the use of LTS_N method [102], Diamond Difference method (DD) [79] and Spectral Green's Function [14]. Further, Dalmolin [40] and Lazzari [68, 69] applied the Nyström method [80] to the same problems, obtaining the same results with good numerical precision. Recently, Lazzari [68,69] applied the same technique to heterogeneous problem, comparing the results obtained with those presented by Garcia and Siewert (F_N method) [53], Schulz (DD) [91] and Prolo and Rodrigues (ADO) [85] showing that the Nyström method can be an option as a way to solve problems with more general characteristics, covering a wider range of situations.

The two-dimensional problem was studied by Loyalka and Tsai who published, in 1975 and 1976, a series of works on the methods used to solve the neutron transport equation at that time [73,101]. In parts II and III, they applied the Nyström method to the two-dimensional heterogeneous problem with and without reflective boundaries.

The Nyström method is a well-established approach for the solution of integral equations that consists of replacing the integral operator in a Fredholm equation of the second kind by a quadrature numerical scheme and producing a linear system to be solved. In such works, numerical results were presented and they concluded that this approach is valid due to the fact that it avoids the ray effect, as well as highlighting the possibility of expanding this method to reflect boundary conditions, multigroup problems, and non-orthogonal geometry. In recent

decades, this approach has been studied again by some research groups, which have applied it to different problems [13, 58, 72, 78, 89].

Other problems in two-dimensional multi-region domains were addressed by Azmy in 1988 [15], who used nodal methods to solve three problems where the number of heterogeneous regions varies from 2 to 4 in domains of different formats and characteristics. Later, Mello and Barros [42] and Barichello [19] studied the same problems using an exponential spectral nodal method and ADO method, respectively. These articles presented more accurate results and advanced the study of these problems, presenting different approaches to such situations.

For three-dimensional (3-D) rectangular problems, Ramankutty and Crosbie [86] applied a modified discrete-ordinate method to solve the three-dimensional rectangular enclosure, which contains an absorbing, emitting and isotropically scattering medium. Furthermore, the authors presented a list of works that had been studied up to that time. Showing the methods that were used for each situation, as well as presenting the open problems for the field.

Still, in three-dimensional problems, Altac and Tekkamaz presented benchmarks for a cubic medium with absorbing and isotropically scattering homogeneous medium using integral methods [6, 7]. Hu and Li [60] solved the same problem using the product integral method, in which the integrand function is replaced by piecewise interpolation polynomial [39, 96]. Anli and Gungor [12] studied two problems in X-Y-Z-cartesian geometry, the first one with a homogeneous medium with isotropic scattering. The second one with two different media and anisotropic scattering, using Spectral Green's Function - Constant nodal method (SGF-CN).

Multi-layered works in the 3-D rectangular domain were developed by Altac and Tekkalmaz, using integral methods combined with the subtraction of singularity technique, solving the radiative transfer problem in absorbing, emitting and isotropically two-layered segregated scattering [9]. A three-layer non-homogeneous

medium case was solved by Tan and Hsu [98], using the discrete rectangular volume (DRV), which is a variation of the general quadrature method [97], and YIX methods [59].

Recently, Azevedo *et al.* [13] and Sauter *et al.* [89] used the Nyström Method combined with the singularity-subtraction technique to solve different classes of two-dimensional problems in X-Y geometry of neutron transport. Although other articles used similar methodologies, in those articles different geometries were addressed as well as semi-reflective boundary conditions were introduced. A situation that had not yet been studied previously. Problems in cylindrical coordinates were also investigated using the same method. Bublitz *et al.* solved transport problems in axisymmetric infinite cylinder [29] and in finite cylinder [30].

In addition to demonstrating that the Nyström Method can be promising, these works show us the need for appropriate mathematical and computational refinements to obtain stable and more accurate numerical results. For example, combine such methods with the use of numerical libraries, code parallelization, as well as numerical substitutions and geometric coordinate changes.

Therefore, this work aims to expand this methodology to more general problems, as well as study mathematical and computational refinements that can be used to obtain efficient and accurate results. More precisely, this work's intention is to study transport problems in two-dimensional in X-Y-cartesian geometry using the Nyström method with the singularity-subtraction technique and computational refinements. In particular, this research presents the study in a nonmultiplying rectangular domain, with multiple regions with different characteristics, i.e., homogeneous and heterogeneous regions, isotropic scattering problems, and isotropic internal source. In addition, the boundary conditions are reflective on two sides of the domain. The results are set side by side with the results available in the literature.

1.1 Objectives

Since the formulation of the transport equation, several works have been developed seeking accurate results with low computational cost. The objective of this work is to present the mathematical formulation, as well as the numerical results obtained using the Nyström method with the singularity-subtraction technique to solve the two-dimensional multi-region problem under different domain conditions, such as in homogeneous or heterogeneous media with isotropic scattering.

The main objective of this work is to advance the pre-existent theory of transport, giving continuity to the works already done by professors Fabio Souto de Azevedo and Esequia Sauter, mainly continuing the work developed in [13] and [89], applying the already developed method studied by them to a more general problem. The main goals are listed below:

1. Present the computational difficulties and complexities in simulating the transport equation due to its multidimensional phase space and integro-differential nature.

2. Apply the Nyström method, along with a singularity-subtraction technique, to solve the two-dimensional fixed-source neutron transport problems.

3. Develop and incorporate strategies, such as domain subregioning, the clipping distance technique, and the manipulation of the Bickley-Naylor function, to simplify the computational process by removing unnecessary calculations and improving the overall solution's precision and efficiency.

4. Demonstrate the effectiveness of the methodology in solving two-dimensional problems involving homogeneous and heterogeneous media with isotropic scattering, highlighting significant advances.

5. Evaluate the performance and versatility of the proposed method by solving several benchmark problems, thus establishing the basis for its applicability to a wider range of transport problems.

1.2 Organization of the Work

This work is divided into six chapters. Here, in the first chapter, a brief introduction to transport problems was presented as a way of motivating the development of this work, as well as its objectives.

The second chapter presents the linear Boltzmann equation in its integral-differential format. The same chapter presents the methods developed and used by several researchers over the years. Among these methods, we briefly describe the probabilistic and deterministic approaches. And, given that this work uses the latter approach, the subsection 2.1.2.1 describes in more detail the Nyström method, which was used here.

The mathematical formulation developed considering the monoenergetic steady-state problem in a nonmultiplying medium with isotropic scattering and isotropic source is presented in Chapter 3. This chapter is followed by Chapter 4, which describes the analytical and numerical techniques that were used together with the Nyström method and the singularity subtraction technique, as well as, the details of the computational implementation.

Finally, Chapter 5 presents the studied problems, as well as numerical results for the scalar flux for each one of them. Furthermore, computational details and comparisons with data available in the literature are provided. In the last chapter, considerations are made including perspectives on future work.

2 THE PARTICLE TRANSPORT EQUATION

The transport equation was first introduced by Ludwig Boltzmann in 1872, in the kinetic theory of gases [28]. Its applications vary from the production of electric energy to even medical applications, therefore, several numerical, and computational studies involve this equation.

Such equation provides a quantitative description of the spatial, directional, energy, and temporal distribution of the particles in material media [24]. Hence, the unknown is a distribution function that depicts the temporal evolution of the particle distribution. In the most general cases, seven independent variables are required to describe the distribution of particles: three spatial coordinates, two angles specifying the particle direction of travel, particle energy, and time [70].

In the case of uncharged particles, e.g., neutrons and photons, the transport process is self-diffusion, i.e., a process in which the particles of interest diffuse through a host or background medium, interacting randomly by way of collision with the microscopic structure of the medium. For instance, diffusion of neutrons through matter, in which the neutrons interact with the nuclei of the host material; the penetration of light through an atmosphere, which involves the interaction of photons with gas atoms or molecules.

In such a situation, the Boltzmann equation reduces to a linear transport equation (or linear Boltzmann equation) [24,48,74]. It describes the relationship between the mechanisms of loss and gain of particles in any given volume of a phase space. Hence, it can be deduced from a particle balance performed in the phase space of the problem. Properties and the derivation of the Boltzmann equation are not going to be presented here. A complete study of its properties and formulation can be found in the works of Pomraning [83], Bell and Glasstone [24], Duderstadt [48] and Ganapol [51].

Several derivations of the neutron transport equation exist, each one with a particular mathematical property facilitating a class of solutions. Among them are integral, even/odd parity, slowing down kernel, multiple collision, invariant embedding, singular integral, Green's function, and pseudo flux [51]. For example, the multiple collision form is appropriate for highly absorbing media. The Green's function representation is best suited for highly heterogeneous 1-D plane media in the multigroup approximation. [51].

In order to state the mathematical formulation for the neutron transport equation, the following assumptions are made:

- Particles may be considered as points;
- Particles travel in straight lines between point collisions;
- Particle-particle interactions may be neglected;
- Collisions may be considered instantaneous;
- The material properties are assumed to be isotropic.
- The properties of nuclei and the compositions of materials are assumed to be known and time-independent;
- Only the expected or mean value of the particle density distribution is considered;

Over those assumptions at any time t, we use six variables to specify the position of any particle in phase space: three position variables denoted by the vector $\mathbf{x}$, the kinetic energy E, and a unit vector Ω, which indicates the direction in which the particle is traveling. With these variables we can define the distribution function $n(\mathbf{x}, \Omega, E, t)$, such that $n(\mathbf{x}, \Omega, E, t)dV d\Omega dE$ is the number of particles in a differential volume element dV about $\mathbf{x}$ traveling in the cone of directions $d\Omega$ about Ω with energies between E and $E + dE$ at time t.

Also, it is conventional in linear transport theory to introduce the angular flux, given by $\Psi(\mathbf{x}, \Omega, E, t) = vn(\mathbf{x}, \Omega, E, t)$ where v is the particle speed. The angular flux is particularly useful since it serves as a starting point for the calculation of neutron reaction rates, flux moments, and other important quantities characterizing the behaviour of neutrons in a medium. For most purposes, the direction that the particles are traveling is irrelevant in calculating reaction rates. Thus, the scalar flux is defined as the integral of the angular flux over all directions [70], i.e.,

$$\Phi(\mathbf{x}, E, t) = \int \Psi(\mathbf{x}, \Omega, E, t) d\Omega. \tag{2.1}$$

It represents the number of neutrons crossing through some arbitrary cross-sectional unit area in all directions per unit of energy and time.

The time-dependent neutron transport equation (without delayed neutron precursors), also called the linear Boltzmann equation, in its integro-differential format, can be written as

$$\begin{aligned}
&\underbrace{\frac{1}{v}\frac{\partial \Psi(\mathbf{x}, \Omega, E, t)}{\partial t}}_{(1)} + \underbrace{\Omega \cdot \nabla \Psi(\mathbf{x}, \Omega, E, t)}_{(2)} + \underbrace{\sigma_t(\mathbf{x}, E)\Psi(\mathbf{x}, \Omega, E, t)}_{(3)} \\
&\qquad = \underbrace{\int_0^\infty \int_{4\pi} \sigma_s(\mathbf{x}, \Omega' \to \Omega, E' \to E)\Psi(\mathbf{x}, \Omega', E', t) d\Omega' dE'}_{(4)} \\
&\qquad + \underbrace{\frac{\chi_p(E)}{4\pi} \int_0^\infty \int_{4\pi} \nu(E')\sigma_f(\mathbf{x}, E')\Psi(\mathbf{x}, \Omega', E', t) d\Omega'}_{(5)} + \underbrace{S(\mathbf{x}, \Omega, E, t)}_{(6)}
\end{aligned} \tag{2.2}$$

where $\chi_p(E)$ is the fission spectrum, that is, the average number of neutrons produced from fission that are born with energy in $[E, E + dE]$, $\nu(E')$ is the average number of neutrons released by fission induced by a neutron of energy E'. $\sigma_t(\mathbf{x}, E)$ and $\sigma_f(\mathbf{x}, E)$ are the macroscopic total cross section and the macroscopic fission cross section, respectively. And, $\sigma_s(\mathbf{x}, \Omega' \to \Omega, E' \to E)$ is the the macroscopic double differential scattering cross section.

The term macroscopic arises from the recognition that it characterizes the probability of neutron interaction in a macroscopic chunk of material (the target), whereas the microscopic cross section characterizes the probability of interaction with only a single nucleus. Also, the macroscopic cross section is the product of the microscopic cross section and the number density characterizing the material. Hence, the macroscopic total cross section characterizes the probability of any interaction with the material and the macroscopic differential scattering cross section represents the probability of scattering from direction Ω' and energy E' to direction range $\Delta\Omega$ and energy range ΔE [51].

The term (1) in Eq. (2.2) represents the time rate of change of particles over the six dimensional "cube" of dimension $dV, d\Omega, dE$. Terms (2) and (3) are loss terms, that is, they mean particles that are been subtracted from the system. The first represents the net leakage rate and the second the collision rate. The remaining terms are related to the gain of particles. The first one, term (4), is linked with the rate at which neutrons scatter into the cube. The fifth term is associated with prompt fission neutrons that are produced in the cube, and the last term is the source of particles.

A simplifying assumption that is often made is to ignore energy dependence altogether, giving the so-called one-speed or monoenergetic form of the transport equation. For this, it is considered that all neutrons can be characterized by a single speed v or kinetic energy $E = \frac{1}{2}mv^2$. Hence, there is no longer any dependence on energy variable [24]. The steady-state case represents the situation where there is no more rate of change of particles, i.e., leading to a stable condition with no time dependence in the particle distribution. Thus, the term (1) is removed from the equation.

A common assumption is that the macroscopic cross sections and/or the source term do not exhibit angular dependence. In such instances, it's described

as isotropic when direction plays no role and anisotropic when there's a directional relation.

Therefore, considering the monoenergetic steady-state problem in a nonmultiplying medium with anisotropic scattering and anisotropic source, the Boltzmann equation can be written as

$$\Omega \cdot \nabla \Psi(\mathbf{x}, \Omega) + \sigma_t(\mathbf{x})\Psi(\mathbf{x}, \Omega) = \int_{S^2} \sigma_s(\mathbf{x}, \Omega' \cdot \Omega)\Psi(\mathbf{x}, \Omega')\, d\Omega' + S(\mathbf{x}, \Omega), \qquad (2.3)$$

where $\Psi(\mathbf{x}, \Omega)$ stands for the angular flux of neutrons in a volume element dV, $d\Omega$ is the incremental solid angle, $\mathbf{x} = (x_1, x_2, x_3)$ is the position vector, $\Omega \in S^2$, S^2 is the two-dimensional unit sphere in $\mathbb{R}^3$, that is, $\Omega = (\Omega_1, \Omega_2, \Omega_3)$, $\Omega_1^2 + \Omega_2^2 + \Omega_3^2 = 1$ where Ω is the direction of travel of the particles,

To solve the transport equation, the flux distribution entering across the surface that surrounds V must be known. Therefore, boundary conditions must be defined. However, such conditions depend on the problem being studied. Among the boundary conditions, there is vacuum boundary condition, i.e., when the particles cross the boundary they no longer influence the domain. Albedo boundary conditions, i.e., the incoming flux on a boundary is set equal to a known isotropic albedo, times the outgoing flux on the same boundary in the direction corresponding to spectral reflection. And reflective boundary condition, i.e., all particles passing out of V over a surface increment return to V.

2.1 Solution Methods to the Transport Equation

The roots of the transport theory go back more than a century to the Boltzmann equation, first formulated for the study of the kinetic theory of gases [28]. However, much of the early development of this theory was stimulated by astrophysical studies of radiant energy transfer in stellar or planetary atmospheres [49].

It was only with the advent of nuclear chain reactors in the 40s that the interest in solving neutral particle transport problems in the broad range of geometrical configurations found in nuclear reactors and radiation shielding applications aroused the interest of researchers. As a result, several analytical methods for the solution of transport problems have been pursued since the 1940s [70]. Some of these methods were described in reactor theory texts, and are also references for new studies to date, for instance, [31, 48, 70, 77].

In addition to the advancement of the mathematical community in the search for analytical solutions, there was a rapid advance in computational processing power. Which provided a change in the community, from problems with only analytical solutions to the search for numerical solutions. Thus, it moved from problems that were limited to very idealized geometric configurations to more realistic and applied problems using computational methods and trying to make the most of the available computational power, in an attempt to produce the most accurate solutions that reproduce the reality of the problems [31].

These numerical methods enable the replication of multiregion and multi-dimensional transport challenges commonly encountered in analyzing nuclear reactors, radiation shields, and other applications. Those methods are the history of two different approaches, commonly called stochastic and deterministic. Stochastic or Monte Carlo methods are based on a probabilistic interpretation of the transport process and do not need the Boltzmann transport equation [63]. In contrast, deterministic methods are based on discretizing the transport equation in each of its independent variables, resulting in an algebraic system of equations, and then solving this algebraic system [31].

Both methodologies were viewed as being incompatible and have been developed independently because each approach has an advantage in certain problems. Thus, both methods have survived and matured. However, during the past 10 years, it has become fairly widely understood that hybrid methods, i.e., methods

that combine aspects of both techniques, can be used to enhance the strengths and overcome the weaknesses of the individual approaches. Although hybrid methods are in the early stages of their development and implementation, when compared with other classical methods, they have already demonstrated that they can yield major improvements in efficiency and accuracy for complex problems [31].

The following subsections present aspects involving both methods, showing the pros and cons as well as how those methods deal with problems with different characteristics.

2.1.1 Probabilistic Methods

As stated above, stochastic methods do not need the Boltzmann transport equation. Instead, they rely only on the detailed physics of interactions between individual neutrons and nuclei. In its simplest form, the Monte Carlo method consists of simulating a finite number of particle histories through the use of a pseudo-random number generator [70]. In each particle history, random numbers are generated and used to sample appropriate probability distributions for scattering angles, track length distances between collisions, and so on.

For instance, consider a fixed source problem in a nonmultiplying medium with only capture and elastic scattering. Assuming that the problem is time-independent, each history begins by sampling the source distribution to determine the particle's initial energy, position, and direction. After stochastically determining the number of mean free paths the particle will travel before colliding, the material region and point of collision are determined. By sampling cross section data, it is determined with which nuclide the particle has collided and whether the collision is a capture or a scattering reaction. If it is captured, the history is terminated, but if it is scattering, the distribution of scattering angles must be sampled to give a new direction. Then, in the case of elastic scattering, a new energy is determined by the

conservation of energy and momentum. With the energy, position, and direction after the collision thus specified the foregoing procedure is repeated for successive collisions until the particle is absorbed or escapes from the system [70].

However, because the number of simulated particles, typically $O(10^7)$, is usually much smaller than the number of physical particles, approx. $O(10^{15})$, Monte Carlo simulations usually have orders of magnitude more statistical noise than the actual physical process. This is an issue when such methods are used to estimate rare events, like the response rate in a detector located far from a source [31].

In contrast, if the geometry of the problem and its cross sections are known, then the results of the Monte Carlo simulation contain only statistical errors. Therefore, by processing a sufficient number of Monte Carlo particles, it is possible to reduce the probable statistical error below any specified level [31].

Monte Carlo methods are widely used because they are relatively easy to implement, their ability to treat complex geometry with great fidelity, and their ability to solve problems accurately with cross-sectional data that can have extremely complex energy dependence. However, Monte Carlo simulations can be costly, both to set up and to run. For instance, to decrease the statistical error by a factor of 10, it is necessary to increase the number of simulated particles by a factor of 100 so it is computationally expensive [31].

Stochastic methods can be extended in a relatively straightforward manner to complex three-dimensional configurations. On the other hand, they are less efficient when the detailed distribution of a dependent variable, such as spatial profiles of flux or power is required. The reason for this is that the flux or other quantities are normally not calculated at a point. Rather the average of it is estimated from the number of collisions, particle track lengths, or some other quantity in some incremental volume $\Delta V \Delta\Omega \Delta E$ of phase space. Hence, if one is looking for a detailed spatial distribution of the scalar flux, the domain of the problem would

have to be divided into many small ΔV and the flux estimated in each of these cells. However, as the ΔV are taken smaller to improve the spatial resolution of the results, the fraction of the number of particle histories contributing to the flux in any one cell decreases rapidly [70].

Therefore, as mentioned previously, the stochastic methods present a great advantage for being able to simulate complex problems in different geometries. However, they also have some problems, such as the difficulties in providing a detailed description of the flux and the high processing time.

2.1.2 Deterministic Methods

Unlike probabilistic methods that seek to simulate the history of several particles and do not require an equation, deterministic methods are based on discretizing the Boltzmann equation in some of its independent variables, and solving the resulting system of algebraic equations [31].

Several methods have been developed for the discretization of the Boltzmann equation over independent variables. For time-dependent problems, the most common method for discretizing the time variable is the implicit, or backward Euler method, due to its simplicity and robustness [106].

Of all the independent variables in the transport equation, the energy variable E is the most problematic. The reason for this is that typically, the material cross sections, and hence the particle flux itself, have an extraordinarily complex energy dependence. For instance, if the energy grid should be chosen for which the solution varies in energy from one grid point to the next by no more than about 15%, then for typical problems, millions of grid points in the energy variable would be required [31].

However, the multigroup method has been developed to deal with this difficulty. This method requires specifying a set of multigroup cross sections, whose values are determined by calculating integrals over the energy of the flux and the flux times the cross section. The best specification of a multigroup cross section depends on the given problem. Also determining accurate problem-dependent multigroup cross sections is the most challenging and time-consuming aspect of deterministic calculations. [31].

Among deterministic methodologies are discrete ordinates method, (or S_N) which is based on discretizing the angular variable and solving a system of ordinary differential equations. Such discretization is made by approximating the integral term in Eq. (2.3) by a numerical quadrature. However, this discretization involves two main challenges: a good choice of discrete directions, for instance, Gauss-Legendre e Gauss-Chebyshev quadrature [50], and an accurate treatment of the spatial variable. After the angular discretization, a system of ordinary differential equations is created and must be solved. Several approaches can be used for this, for example, Diamond Difference [15], Spectral Green Function [44], Arbitrarily High Order Transport [23], Finite Element Method [62], and Finite Volume Methods [77].

However, discrete ordinates or discrete-ordinates like methods display computational anomalies called *ray effects*. This is due to the discretization of the angular variables along a few discrete characteristics, i.e., rays. So the solutions contain spatial ripples that are not accounted for the physics of the problem [10, 48]. This difficulty arises in problems that tend to have very different characteristics, like those with very little if any scattering, and localized sources [70]. Therefore, it was the subject of several researches at the beginning of the development of discrete ordinate methods [65, 66].

Due to this difficulty, some methods were developed, among them the method proposed by Barrichello and Siewert, called Analytical Discrete Ordinates

(ADO) [22]. Such method consists of constructing the homogeneous solution of the associated problem in terms of separation constants and eigenfunctions, which are defined by expressions involving eigenvalues and eigenvectors, the solution being obtained analytically in the spatial variable [37]. Therefore, in this approach, the solution of the transverse integrated one-dimensional equations are explicitly written in terms of the spatial variables, and the general solutions are obtained from a spectral method where the associated eigenvalue problem is of reduced order, to only half of the number of discrete directions [38]. The ADO method has proved to be very efficient in solving multidimensional transport problems as described in [20, 21, 23, 38, 82, 100].

Differently from the discrete ordinates technique, integral methods are based on integrating the angular dependence from the transport equations. For isotropic scattering, the result is an integral equation in space variables only. This leaves one to deal with the scalar flux and, in some cases, the expected number of particles crossing cell boundaries [10].

The positive aspect of such methods is that by integrating the angular dependence one can in principle treat the angular variable with high accuracy, that is, the results will not change due to the ray effect. However, the treatment of the spatial variables leads to dense matrices which result in severe limitations on the number of spatial grid points that can not be treated due to limitations in computer memory and runtime. Therefore, for most practical problems, it is necessary to use iterative methods to calculate solutions, since the calculation of the inverse of a matrix is computationally expensive and, sometimes, infeasible [55].

Among the integral methods, two methodologies that provided good results can be highlighted: the Synthetic Kernel method [4, 5, 45, 46, 99] and, more recently, the Nyström method [13, 29, 30, 89]. The Synthetic Kernel method, or SK_N, [3, 10, 94] relies on approximating the integral transport kernels by a sum of diffusion-like kernels that preserve spatial moments of the kernels, i.e., replacing

the kernels which are generally integral functions by Gaussian summation over the integration parameter [10].

The Nyström method was developed by Evert Johannes Nyström in 1930 [80]. The method consists of replacing the integral operator by a quadrature numerical scheme, producing a linear system to be solved. In 1975 and 1976, Tsai and Loyalka [71, 73] drew attention to the application of the Nyström method with the singularity-subtraction technique to the integral formulation of the transport equation in a seminal series of notes discussing the best way to solve the neutron transport equation at those times.

In recent works, the Nyström method has been applied to solve transport problems in different geometries. The one-dimensional case of the transport equation, considering homogeneous domain and semi-reflective boundary conditions, was solved by Dalmolin et al. [40]. The solution to this problem in two-dimensional Cartesian geometry was presented by Azevedo *et al.* [13] and by Sauter *et al.* [89]. The first work presented the numerical solution for the transport integral equation with a vacuum boundary condition, while the second generalizes to semi-reflective boundary conditions.

In addition, several results in cylindrical geometry were published by Bublitz *et al.* using the same technique [29, 30]. The first work presented results for the infinitely long axisymmetric cylinder case, and the last one for the finite cylinder case, both with isotropic scattering.

2.1.2.1 Nyström Method

The transport equation, in its integral formulation, is a Fredholm equation of the second kind [24], which is a type of equation whose analytical solutions are rarely possible to obtain [10]. As a way of seeking a numerical result for transport problems, the Nyström method can be applied to this equation. This subsection

presents the main idea of the method for a generic Fredholm equation, the development of it for the transport equation will be presented in the following chapter.

The Nyström method [80], consists of approximating the integral over a domain by a selected numerical quadrature scheme [43, 84]. That is,

$$\int_a^b K(t,s)\phi(s)ds = \sum_{j=1}^{N} w_j K(t,s_j)\phi(s_j) \tag{2.4}$$

where $\{w_j\}_{j=1}^N$ are the weights and $\{s_j\}_{j=1}^N$ are the nodes of the numerical quadrature scheme. This method is commonly applied to Fredholm equations [92].

An inhomogeneous Fredholm equation of the second kind is given by

$$\phi(t) = y(t) + \lambda \int_a^b K(t,s)\phi(s)ds \tag{2.5}$$

or, in operational notation, $(1-\lambda L)\phi = y$, where L is the integral operator of (2.5). This operator equation has a solution ϕ whenever the operator $1-\lambda L$ is invertible and this inversion may be done in different functional spaces [13]. Therefore, by applying the Nyström method in the Fredholm equation, the following linear system with N variables is produced and its solution provides the function ϕ in the quadrature points s_j.

$$\begin{bmatrix} 1-\lambda w_1 K(s_1,s_1) & -\lambda w_2 K(s_1,s_2) & \cdots & -\lambda w_N K(s_1,s_N) \\ -\lambda w_1 K(s_2,s_1) & 1-\lambda w_2 K(s_2,s_2) & \cdots & -\lambda w_N K(s_2,s_N) \\ \vdots & \vdots & \ddots & \vdots \\ -\lambda w_1 K(s_N,s_1) & -\lambda w_2 K(s_N,s_2) & \cdots & 1-\lambda w_N K(s_N,s_N) \end{bmatrix} \begin{bmatrix} \phi(s_1) \\ \phi(s_2) \\ \vdots \\ \phi(s_N) \end{bmatrix} = \begin{bmatrix} y(s_1) \\ y(s_2) \\ \vdots \\ y(s_N) \end{bmatrix} \tag{2.6}$$

However, in many cases, the kernel K of the integral operator has singularity along the line $t = s$. This singularity can cause noises during numerical computation, generating incorrect results. Therefore, a simple strategy to deal with the singularity is the singularity-subtraction technique [43, 84], which consists of

rewriting the integral operator as

$$\int_a^b K(t,s)\phi(s)ds = \int_a^b K(t,s)[\phi(s)-\phi(t)]ds + \phi(t)\int_a^b K(t,s)ds. \tag{2.7}$$

Doing this, the first term on the right side of the previous equation is now regular at $t = s$, that is, provided that the original integral existed in the Riemann sense. Due to the fact that, it is less singular than the original form, since $\phi(s) - \phi(t) = 0$ over the assumed singular point. Then, the Nyström method can be applied to expand the integral and produce a linear system, which is similar to the one presented in Eq. (4.11). Yet, even with the removal of the singularity, the integral of the kernel needs to be calculated. However, in some cases, it has an analytical representation, which makes possible for it to be rewritten based on equations that are already known and easy to compute [34]. Otherwise, it is possible to continue the subtraction process further in a systematic way, to smooth out the equation.

3 MATHEMATICAL FORMULATION OF THE PROBLEM

Considering the monoenergetic steady-state problem in a nonmultiplying medium with isotropic scattering and isotropic source, the Boltzmann equation can be written as

$$\Omega \cdot \nabla \Psi(\mathbf{x}, \Omega) + \sigma_t(\mathbf{x}) \Psi(\mathbf{x}, \Omega) = \frac{\sigma_s(\mathbf{x})}{4\pi} \int_{S^2} \Psi(\mathbf{x}, \Omega') d\Omega' + S(\mathbf{x}), \tag{3.1}$$

where $\mathbf{x} = (x_1, x_2, x_3) \in D \times \mathbb{R}$, $D = [0, a] \times [0, b]$, Ω is the direction-of-flight vector, a unit vector ($|\Omega| = 1$), in the unit sphere in S^2, and $\nabla \Psi(\mathbf{x}, \Omega) = \frac{\partial \Psi}{\partial x_1} \vec{i} + \frac{\partial \Psi}{\partial x_2} \vec{j}$. $S(\mathbf{x})$ is the internal isotropic neutrons source term defined in $[0, a_s] \times [0, b_s]$, and $\sigma_t(\mathbf{x})$ and $\sigma_s(\mathbf{x})$ are the total and scattering macroscopic cross sections, respectively.

The multi-region case is considered, so the domain D is decomposed as the union of almost disjoint regions R_i, i.e., the interiors of the rectangles are disjoint, as represented in Figure 3.1. Furthermore, the functions $\sigma_t(\mathbf{x})$ and $\sigma_s(\mathbf{x})$ are constant inside each rectangle R_i.

To complete the statement of the problem, we impose vacuum boundary conditions on the right and top boundaries of the domain and reflective boundary conditions on the left and bottom boundaries of the domain. Such a spatial configuration was proposed and used in several works [8, 15, 73]. Mathematically the boundary conditions are given by

$$\Psi(\mathbf{x}, \Omega) = \beta \Psi(\mathbf{x}, \Omega'), \quad \mathbf{n} \cdot \Omega < 0, \quad \mathbf{x} \in \partial D \times \mathbb{R}. \tag{3.2}$$

Here, $\beta = 0$ if $\mathbf{x}$ is on the right or top boundaries and $\beta = 1$ if $\mathbf{x}$ is on the bottom or left boundaries. And, Ω' is the reflection angle corresponding to an incident angle of Ω on the boundary, $\mathbf{n}$ is the outer unit normal vector, $\mathbf{n} \cdot \Omega = -\mathbf{n} \cdot \Omega'$ and $(\Omega \times \Omega') \cdot \mathbf{n} = 0$ [70].

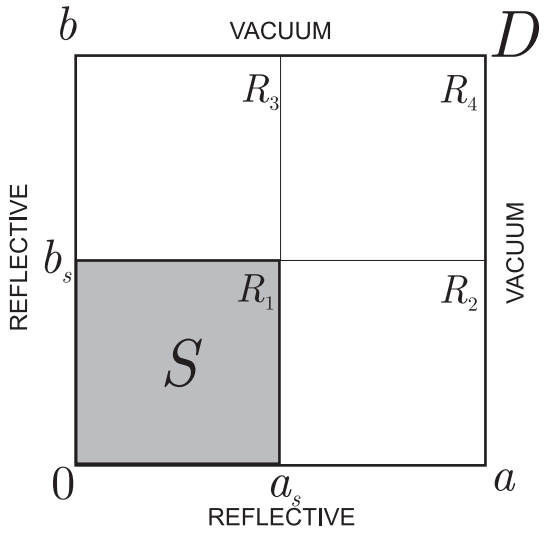

Figure 3.1: Representation of domain D, where the R_i's are regions of D, and S is the internal isotropic source.

3.1 Integral formulation

In this section, the integral formulation for the problem established at the beginning of this chapter is presented. First, the auxiliary case where the boundaries do not have reflection is considered. Later, the more general situation involving two reflective boundaries is examined.

3.1.1 Integral formulation for the basic problem

Representing the right-hand side of Eq. (3.1) as $Q(\mathbf{x})$ and applying the method of characteristics [24, 35, 77] it is possible to obtain the following representation for the unknown $\Psi(\mathbf{x}, \Omega)$:

$$\Psi(\mathbf{x}, \Omega) = \int_0^{s(\mathbf{x},\Omega)} Q(\mathbf{x} - r\Omega) e^{-\int_0^r \sigma_t(\mathbf{x}-s\Omega)ds} dr, \tag{3.3}$$

where $s(\mathbf{x}, \Omega) = \sup_{s>0} \{s : \mathbf{x} - s\Omega \in D \times \mathbb{R}\}$.

By using the previous equation and the definition of scalar flux, Eq. (2.1), it can be rewritten as

$$\Phi(\mathbf{x}) = \frac{1}{4\pi}\int_{S^2}\int_0^{s(\mathbf{x},\Omega)} Q(\mathbf{x}-r\Omega)e^{-\int_0^r \sigma_t(\mathbf{x}-s\Omega)ds}drd\Omega. \tag{3.4}$$

Applying the change of variables $\mathbf{y} = \mathbf{x} - r\Omega$ and using the volume element in spherical coordinates, $dy = r^2 drd\Omega$, the following expression is derived:

$$\Phi(\mathbf{x}) = \frac{1}{4\pi}\int_{D\times\mathbb{R}} Q(\mathbf{y})\frac{e^{-\Lambda(\mathbf{x},\mathbf{y})}}{|\mathbf{x}-\mathbf{y}|^2}d\mathbf{y} \tag{3.5}$$

$$= \frac{1}{4\pi}\int_{-\infty}^{\infty}\int_D Q(\mathbf{y})\frac{e^{-\Lambda(\mathbf{x},\mathbf{y})}}{|\mathbf{x}-\mathbf{y}|^2}d\mathbf{y} \tag{3.6}$$

$$= \frac{1}{2\pi}\int_{0}^{\infty}\int_D Q(\mathbf{y})\frac{e^{-\Lambda(\mathbf{x},\mathbf{y})}}{|\mathbf{x}-\mathbf{y}|^2}d\mathbf{y}, \tag{3.7}$$

where the function $\Lambda : D \times D \to \mathbb{R}_+$ is given by

$$\Lambda(\mathbf{x},\mathbf{y}) = |\mathbf{x}-\mathbf{y}|_2\int_0^1 \sigma_t\left((1-t)\mathbf{x}+t\mathbf{y}\right)dt \tag{3.8}$$

with $|\mathbf{x}-\mathbf{y}|_2 = \sqrt{(x_1-y_1)^2+(x_2-y_2)^2}$.

Note that $\Lambda(\mathbf{x},\mathbf{y})$ essentially represents a linear interpolation, that is, we are evaluating $\sigma_t(\mathbf{x})$ along a segment between two points. In this case, for a given fixed point $\mathbf{x}$, the integral in Eq. (3.8) evaluates the σ_t values along the segment that connects $\mathbf{x}$ to $\mathbf{y}$, where $\mathbf{y}$ is the integration variable over the entire domain D.

Defining the cosine of the elevation angle η as

$$\eta = \frac{\sqrt{(x_1-y_1)^2+(x_2-y_2)^2}}{\sqrt{(x_1-y_1)^2+(x_2-y_2)^2+(x_3-y_3)^2}} = \frac{|\mathbf{x}-\mathbf{y}|_2}{|\mathbf{x}-\mathbf{y}|}, \tag{3.9}$$

the expression (3.7) is rewritten as

$$\Phi(\mathbf{x}) = \frac{1}{2\pi}\int_0^1\int_D Q(\mathbf{y})\frac{e^{-\frac{\Lambda(\mathbf{x},\mathbf{y})}{\eta}}}{\sqrt{1-\eta^2}|\mathbf{x}-\mathbf{y}|_2}dy_1dy_2d\eta \tag{3.10}$$

$$= \frac{1}{2\pi}\int_D \frac{Q(\mathbf{y})}{|\mathbf{x}-\mathbf{y}|_2}\int_0^1 \frac{e^{-\frac{\Lambda(\mathbf{x},\mathbf{y})}{\eta}}}{\sqrt{1-\eta^2}}d\eta dy_1dy_2 \tag{3.11}$$

$$= \int_D Q(\mathbf{y})k(\mathbf{x},\mathbf{y})d\mathbf{y}, \tag{3.12}$$

where

$$k(\mathbf{x},\mathbf{y}) = \frac{1}{2\pi}\frac{1}{|\mathbf{x}-\mathbf{y}|_2}\int_0^1 \frac{e^{-\frac{\Lambda(\mathbf{x},\mathbf{y})}{\eta}}}{\sqrt{1-\eta^2}}d\eta. \tag{3.13}$$

This last equation, Eq. (3.13), is named kernel of the integral. However, transforming integrals into known forms using tabulated functions enhances computational efficiency and accuracy by simplifying complex calculations and using precomputed values. One of the known functions are the Bickley-Naylor functions [26,27], which can be defined in different ways, as presented by Altaç [2]. The first order Bickley-Naylor function can be defined by

$$\mathrm{Ki}_1(r) = \int_0^1 \frac{e^{\frac{-r}{x}}}{\sqrt{1-x^2}}dx. \tag{3.14}$$

Using the previous equation, is possible to simplify Eq. (3.13) as

$$k(\mathbf{x},\mathbf{y}) = \frac{1}{2\pi}\frac{\mathrm{Ki}_1(\Lambda(\mathbf{x},\mathbf{y}))}{|\mathbf{x}-\mathbf{y}|_2}. \tag{3.15}$$

Defining the integral operator L_g over a function f as follows

$$(L_g f)(\mathbf{x}) = \int_D f(\mathbf{y})k(\mathbf{x},\mathbf{y})d\mathbf{y} \tag{3.16}$$

and using the definition of $Q(\mathbf{x})$, the scalar flux can be expressed as

$$\Phi = L_g\left(\sigma_s\Phi + S\right), \tag{3.17}$$

which is equivalent to

$$(1 - L_g\sigma_s)\Phi = L_g S. \tag{3.18}$$

This operational equation has a solution Φ whenever the operator $1 - L_g\sigma_s$ is invertible. Due to the fact that $\|L_g\sigma_s\| < 1$ in $L^2(D)$ and $L^\infty(D)$ spaces, when $\sigma_s < \sigma_c$, where σ_c is the inverse of the largest eigenvalue of L_g in $L^2(D)$ [13,105], the operator is invertible and this last equation can be rewritten as

$$\Phi = (1 - L_g\sigma_s)^{-1}L_g S. \tag{3.19}$$

3.1.2 Integral formulation for the general problem

In order to deal with the general problem, which consists of the case where the bottom and the left boundary are reflective, the same approach used for the basic problem can be applied. Using a mirror technique and expanding the domain beyond the original boundaries it is possible to deal with such case. Figure 3.2 represents the new domain.

Considering a fixed point $\mathbf{x}$ in D the scalar flux in $\mathbf{x}$ is calculated through an integral in $\mathbf{y}$ in which the integration domain is the entire domain and its reflections, see Eqs. (3.10) and (3.15). Therefore, the contribution of the reflection of the point $\mathbf{y}$ through the bottom and the left boundary for $\mathbf{x}$ can be calculated using as reference the point $\mathbf{y'}$. Also, notice that the distance d_1 traveled inside the region R_1 is the same as d_1' inside the region R_1' which is the reflection of R_1, so it has the same characteristics. The same idea can be applied to the distance d_2 but now inside of R_2'.

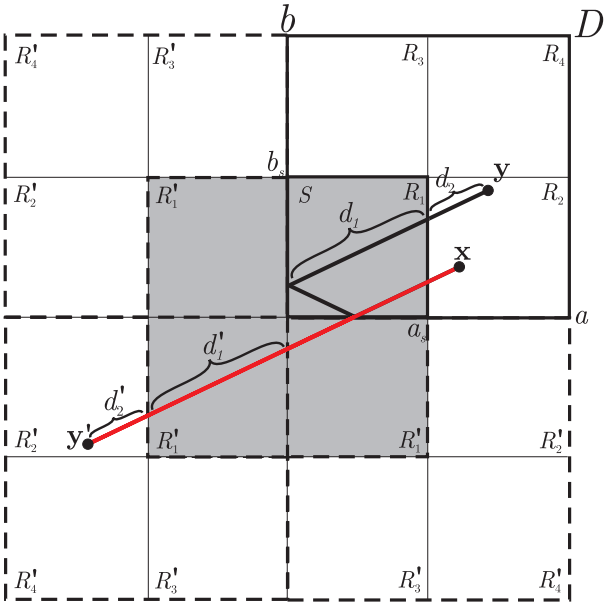

Figure 3.2: The expanded domain for the general problem.

Consequently, for each of the points of a mesh in the domain D, the contribution of each of the other points of the extended domain must be calculated. However, due to the singularity when $\mathbf{x}$ and $\mathbf{y}$ are in the same region, it is necessary to give it an effective treatment in order to produce more accurate results. Such analysis will be described in the following chapter.

4 NUMERICAL TECHNIQUES AND IMPLEMENTATION

As a way to produce more accurate results, several analytical and numerical techniques were combined in the code developed in this work. Among them are the refinement of the domain in subregions, the singularity-subtraction technique, the choice of a numerical quadrature, the Neumann series, the change of variable over Bickley-Naylor function, and a *clipping distance* technique. This chapter presents and discusses those computational methods and strategies in the following sections.

4.1 Subregions

This concept of subregions is based on the idea of refining each part of the domain into $N_R \times N_R$ smaller regions, as shown in Figs. 4.1a - 4.1c. The original domain is said $N_R = 1$ due to the fact that there is only one interval in each region, as represented in Fig. 4.1a. Each region in Fig. 4.1a can be divided into four regions, as represented in Fig. 4.1b. These new regions inherit the characteristics of their respective region in Fig. 4.1a, and, it is said that $N_R = 2$ for this domain. The domain can also be divided into more regions, as represented in Fig. 4.1c where $N_R = 5$, i.e., the region segment was divided into 5 segments, and so on for any desired amount of subregions.

The advantage of using subregions is twofold, firstly the new integration regions are smaller, which speeds up the numerical process considering that precise integration over large domains has a high computational cost. Second, the numerical quadrature type and the amount of quadrature points can be chosen specifically for each mesh. Thus, subregions can have their meshes refined without the need to increase the number of points in the entire domain, named submeshes. Decreasing

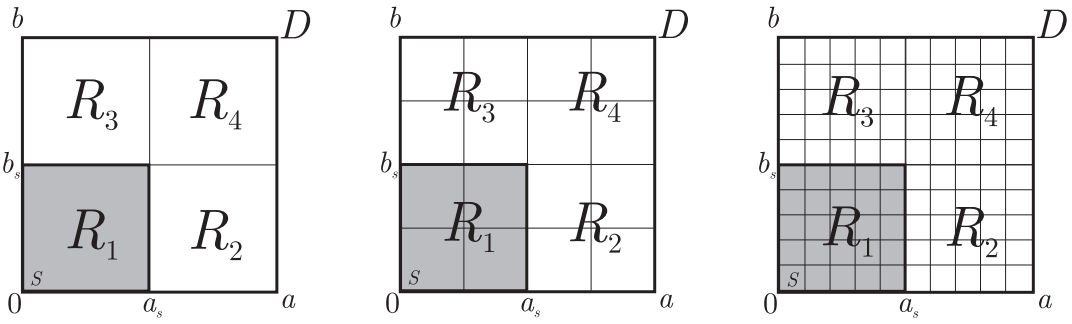

(a) $N_R = 1$. (b) $N_R = 2$. (c) $N_R = 5$.

Figure 4.1: Representation of the division of domain D into $N_R \times N_R$ subregions.

the number of points in regions where there is no need for such fine refinement, consequently decreases the computational time.

In addition to the number of subregions into which each domain is divided, another variable was created in order to provide greater precision and automate the construction of quadrature schemes for each subregion. Such a variable called Δ, is related to the number of points in each submesh. Thus, each subregion has its own mesh, called a submesh, which is of size $N_i \times N_i$, base on the following equation.

$$N_i = 1 + w_N \left\lceil \frac{(\text{length})_i \cdot \Delta \cdot \sigma_{tR}}{w_N} \right\rceil \tag{4.1}$$

where N_i is the amount of points in i direction (x or y direction), w_N is the order of a quadrature rule, $(\text{length})_i$ is the length of the subregion in the i direction and σ_{tR} is the total macroscopic cross section of the region R.

Note that the number of points depends on the total macroscopic cross section of the region, thus, the larger the cross section, the greater the number of points in that region. Therefore, the choice of a Δ depends on the characteristics of the problem, such as domain size and cross-sections, as well as the desired numerical precision. More details will be discussed in Chapter 5, Numerical Results.

4.2 Singularity-subtration technique over a numerical quadrature

Although the kernel of the integral operator L_g, Eq. (3.16), has been redefined using the Bickley-Naylor equation, forming the expression presented in Eq. (3.15), it still has singularity whenever $\mathbf{x} = \mathbf{y}$. That is, for a point $\mathbf{x} \in D$, the integral operator L_g works on the kernel integrating over the entire domain D, so, at some point, the integral will pass through the point $\mathbf{x}$, which will make the denominator equal to zero. Thus, it will create a singularity and numerical errors may occur.

Therefore, the singularity removal technique, discussed in Session 2.1.2.1, can be applied here as a way to obtain better results. Furthermore, due to the additivity property of the integral and the use of subregions, described in the previous section, instead of applying an integration over the entire domain D, this domain can be divided into multiple smaller subregions, and operate with the removal technique only in the region where $\mathbf{x}$ is located.

Hence, the operator L_g over any function $q(\mathbf{x})$ can be expanded as the following equation.

$$(L_g q)(\mathbf{x}) = \int_D k(\mathbf{x},\mathbf{y}) q(\mathbf{y}) d\mathbf{y} \tag{4.2}$$

$$= \sum_{R \in D : \mathbf{x} \notin R} \int_R k(\mathbf{x},\mathbf{y}) q(\mathbf{y}) d\mathbf{y} + \sum_{R \in D : \mathbf{x} \in R} \int_R k(\mathbf{x},\mathbf{y})(q(\mathbf{y}) - q(\mathbf{x})) d\mathbf{y}$$

$$+ q(\mathbf{x}) \sum_{R \in D : \mathbf{x} \in R} \int_R k(\mathbf{x},\mathbf{y}) d\mathbf{y}. \tag{4.3}$$

The first term on the right side of Eq. (4.3) represents the contribution of all the regions except for the regions where $\mathbf{x}$ is located. The contribution for the region where $\mathbf{x}$ is located is given by the second and the third terms. For instance, considering the case presented in Figure 4.1a, the first term computes all the regions R_i, for $i = 1, 2, 3, 4$, except for R_i where the $\mathbf{x}$ is, which is computed by the other

components. Besides that, notice that a point $\mathbf{x}$ can be in one, two, or four regions at the same time, for example, on the border between R_1 and R_2, or even in the center of the domain. Therefore, the amount of terms in each sum varies depending on $\mathbf{x}$, so this must be taken into account during computational implementation.

In order to calculate numerically the integrals in Eq. (4.3), the Nyström method can be used. As previously described, the first part of such a method consists of replacing the integral of the equation by a selected numerical quadrature scheme. Applying such approach, the previous equation can be written as

$$\begin{aligned}(L_g q)(x_{ij}) = &\sum_{R\in D: x_{ij}\notin R}\sum_{x_{ij}\neq x_{lm}} w_{lm}k(x_{ij},x_{lm})q(x_{lm}) \\ &+ \sum_{R\in D: x_{ij}\in R}\sum_{x_{ij}\neq x_{lm}} w_{lm}k(x_{ij},x_{lm})(q(x_{lm})-q(x_{ij})) \\ &+ q(\mathbf{x})K_{ij} \end{aligned} \tag{4.4}$$

where x_{lm} and $w_{l,m}$, $1 \leq l \leq N$ and $1 \leq m \leq N$, are nodes and weights of a numerical quadrature, respectively, and

$$K_{ij} = \sum_{R\in D: x_{ij}\in R}\int_R k(\mathbf{x}_{ij},\mathbf{y})d\mathbf{y} \tag{4.5}$$

where the integrand is the same as Eq. (3.15).

4.3 Numerical quadrature

As a way of establishing a numerical quadrature that did not use extreme points, we chose to construct a numerical quadrature, of order 4, with equally spaced nodes, but with the first and last nodes at a distance of half the step from the extremes. The idea of using a different spacing for the extreme nodes comes from the fact that, although the distance to the extremes is $h/2$, the distance between the last and first nodes continues to be h.

To calculate the weights w_i of this quadrature, we can write the Lagrange polynomials at each of these nodes. Each Lagrange polynomial $L_i(x)$ is defined for a set of points $x_0, ..., x_n$, where each $L_i(x)$ is constructed to equal 1 at point x_i and 0 at all other points x_j, with $j \neq i$. This means that $L_i(x)$ reaches the maximum value at the corresponding sampling point and is zero elsewhere, ensuring that each point has its unique contribution to the interpolation of the function. The general form of a Lagrange polynomial is:

$$L_i(x) = \prod_{\substack{j=0 \\ j \neq i}}^{n} \frac{x - x_j}{x_i - x_j} \tag{4.6}$$

where the product is calculated over all j except i, and n is the total number of points minus one.

Consider the construction of this quadrature in the interval $[0, 1]$. So five nodes are $x_0 = \frac{h}{2}$,$x_1 = \frac{3h}{2}$,$x_2 = \frac{5h}{2}$,$x_3 = \frac{7h}{2}$, and $x_4 = 1 - \frac{h}{2}$. Also, $h = \frac{1}{5}$. Thus, the Lagrange polynomials are given by:

$$L_0(x) = \frac{625x^4}{24} - \frac{125x^3}{2} + \frac{2575x^2}{48} - \frac{155x}{8} + \frac{315}{128} \tag{4.7a}$$

$$L_1(x) = -\frac{625x^4}{6} + \frac{1375x^3}{6} - \frac{1025x^2}{6} + \frac{1145x}{24} - \frac{105}{32} \tag{4.7b}$$

$$L_2(x) = \frac{625x^4}{4} - \frac{625x^3}{2} + \frac{1625x^2}{8} - \frac{375x}{8} + \frac{189}{64} \tag{4.7c}$$

$$L_3(x) = -\frac{625x^4}{6} + \frac{375x^3}{2} - \frac{325x^2}{3} + \frac{185x}{8} - \frac{45}{32} \tag{4.7d}$$

$$L_4(x) = \frac{625x^4}{24} - \frac{125x^3}{3} + \frac{1075x^2}{48} - \frac{55x}{12} + \frac{35}{128} \tag{4.7e}$$

Once the Lagrange polynomials have been determined, they can be integrated over the interval $[0, 1]$ to find the respective quadrature weights. That is, integrating each of the previous equations, Eq. (4.7), in the previously chosen interval, we produce the respective weights w_i, which are:

$$w_0 = \tfrac{1375}{1152} \quad w_1 = \tfrac{125}{288} \quad w_2 = \tfrac{335}{192} \quad w_3 = \tfrac{125}{288} \quad w_4 = \tfrac{1375}{1152}$$

Thus, the integral over a function f, using the newly defined quadrature, can be expressed as

$$\int_0^1 f(x)dx = \frac{5}{1152}h(275f(x_0)+100f(x_1)+402f(x_2)+100f(x_3)+275f(x_4)), \quad (4.8)$$

where x_i and h are as previously defined.

4.4 Neumann Series

The Neumann series, named after the mathematician Carl Neumann, originated in 1877 within the realm of potential theory [103]. It serves as a foundational concept in functional analysis, particularly in the study of linear operators. It forms the basis of the Liouville-Neumann series, which is used to solve Fredholm integral equations [92].

A Neumann series is a mathematical series of the form

$$\sum_{k=0}^{\infty} T^k$$

where T is an operator and $T^k := T^{k-1} \circ T$ its k times repeated application.

This series provides a systematic approach to approximate solutions for equations involving linear operators, contributing significantly to various fields of mathematics and its practical applications. One of its properties states: Suppose T is a bounded linear operator on the normed vector space X. If the Neumann series converges in the operator norm, then $\mathrm{Id} - T$ is invertible and its inverse is the series:

$$(\mathrm{Id} - T)^{-1} = \sum_{k=0}^{\infty} T^k \quad (4.9)$$

where Id is the identity operator in X.

Remember that scalar flux is represented by Eq. (3.18), i.e.,

$$(1 - L_g\sigma_s)\Phi(\mathbf{x}) = L_g S(\mathbf{x}). \quad (4.10)$$

Thus, the approximated scalar flux in a mesh point can be obtained by solving the linear system

$$(1 - L_g\sigma_s)\Phi(\mathbf{x}_{ij}) = (L_gS)(\mathbf{x}_{ij}) \tag{4.11}$$

or

$$\Phi(\mathbf{x}_{ij}) = (1 - L_g\sigma_s)^{-1}(L_gS)(\mathbf{x}_{ij}). \tag{4.12}$$

The discrete version of $(L_g)(\mathbf{x}_{ij})$ produces a large matrix, which can increase processing time and lead to problems with computational storage. Thus, in order to avoid those situations, iterative methods can be used as an alternative to direct solvers. Iterative methods attempt to solve linear systems by progressively iterating over an initial guess until a stopping criterion is achieved. These methods are more efficient in terms of memory usage and computational resources when compared to direct solvers, since they only require the storage of intermediate results at each iteration, rather than the complete solution matrix.

Thus, as $(1-L_g\sigma)$ is invertible [13], the iterative process of the Neumann Series was chosen due to its stability and low memory cost [92, 104]. In this case, the scalar flux at each point of a mesh can be written as

$$\begin{aligned}\Phi(\mathbf{x}_{ij}) &= (1 - L_g\sigma_s)^{-1}(L_gS)(\mathbf{x}_{ij}) &(4.13)\\ &= \sum_{n=0}^{\infty} \sigma_s^n L_g^n (L_gS)(\mathbf{x}_{ij})\\ &\approx \sum_{n=0}^{M} \sigma_s^n T_{ij}^n(\mathbf{x}_{ij}) + \frac{\sigma_s^{M+1}\sigma_c}{1-\sigma_s\sigma_c} T_{ij}^M, &(4.14)\end{aligned}$$

where

$$T_{ij}^0 = \sum_{R\in D:\mathbf{x}\notin R} \int_R k(\mathbf{x},\mathbf{y})S(\mathbf{y})d\mathbf{y} + \sum_{R\in D:\mathbf{x}\in R} \int_R k(\mathbf{x},\mathbf{y})(S(\mathbf{y}) - S(\mathbf{x}))d\mathbf{y} \quad + S(\mathbf{x}_{ij})K_{ij}. \tag{4.15a}$$

$$T_{ij}^{n+1} = \sum_{R\in D: x_{ij}\notin R} \sum_{l,m} w_{lm} k(x_{ij}, x_{lm}) T_{kl}^{n}$$

$$+ \sum_{R\in D: x_{ij}\in R} \sum_{x_{ij}\neq x_{lm}} w_{lm} \left[T_{lm}^{n} - T_{ij}^{n}\right] k(\mathbf{x}_{ij}, \mathbf{x}_{lm}) + T_{ij}^{n} K_{ij}, \quad n \geq 0 \tag{4.15b}$$

where,

$$K_{ij} = \sum_{R\in D: x_{ij}\in R} \int_R \frac{1}{2\pi} \frac{\mathrm{Ki}_1(\Lambda(x_{ij}, \mathbf{y}))}{|x_{ij} - \mathbf{y}|_2}, \tag{4.16}$$

and $1/\sigma_c$ is approximated by the Rayleigh quotient [105]

$$1/\sigma_c \approx \frac{\left\langle T_{ij}^{M-1}, T_{ij}^{M} \right\rangle}{\left\langle T_{ij}^{M-1}, T_{ij}^{M-1} \right\rangle}, \tag{4.17}$$

with $\langle \mathbf{u}, \mathbf{v} \rangle$ being the inner product of functions in L^2 space.

Furthermore, as can be seen in Eq. (4.14), the i-th term of the series must be multiplied by σ_s, raised to the i-th power. Thus, as the number of terms increases, the exponent increases, and the smaller the σ_s value is, the faster the series converges. Therefore, the lower the σ_s value, the fewer terms in the series are needed. Using this idea, it is possible to estimate how many series terms are needed for convergence and produce an efficient code.

Although this iterative process provides the scalar flux only at mesh points, the following equation can be used in order to approximate the flux at any point of the medium using the values already computed. This interpolation was derived from Eq. (4.11) using the operator discretization described in Eq. (4.4).

$$\Phi(\mathbf{x}) = \frac{A + B}{C} \tag{4.18}$$

where

$$A = \sum_{R\in D: \mathbf{x}\notin R} \sigma_s^R \sum_{i,j} w_{ij} k(\mathbf{x}, y_{i,j}) \Phi(y_{ij}) + \sum_{R\in D: \mathbf{x}\in R} \sigma_s^R \sum_{ij, \mathbf{x}\neq y_{ij}} w_{i,j} k(\mathbf{x}, y_{ij}) \Phi(y_{ij}) \tag{4.19}$$

$$B = \sum_{R\in D: \mathbf{x}\notin R} \sum_{i,j} w_{ij} k(\mathbf{x}, y_{ij}) S(y_{ij}) + \sum_{R\in D: \mathbf{x}\in R} \sum_{ij, \mathbf{x}\neq y_{ij}} w_{ij} k(\mathbf{x}, y_{ij}) (S(y_{ij}) - S(\mathbf{x}))$$

$$+ S(\mathbf{x}) \sum_{R\in D: \mathbf{x}\in R} \int_R k(\mathbf{x}, \mathbf{y}) d\mathbf{y} \tag{4.20}$$

$$C = 1 + \sum_{R \in D : \mathbf{x} \in R} \sigma_{sR} \sum_{ij, \mathbf{x} \neq y_{ij}} w_{ij} k(\mathbf{x}, y_{ij}) - \sum_{R \in D : \mathbf{x} \in R} \sigma_{sR} \int_R k(\mathbf{x}, \mathbf{y}) d\mathbf{y} \tag{4.21}$$

where σ_{sR} is the scattering macroscopic cross sections of the region of the respective summation.

4.5 Change of variable over Bickley-Naylor function

Although it was possible to write a representation for the scalar flux by an iterative method using the Neumann series, it is still necessary to compute the sum in Eq. (4.14) using Eqs. (4.15a) and (4.15b). Furthermore, although the integrals have been expanded by numerical quadratures, the term K_{ij}, defined in Eq. (4.16), continues to depend on a two-dimensional numerical integration. That is,

$$K_{ij} = \sum_{R \in D : x_{ij} \in R} \int_R \frac{1}{2\pi} \frac{\mathrm{Ki}_1(\Lambda(x_{ij}, \mathbf{y}))}{|x_{ij} - \mathbf{y}|_2} d\mathbf{y}. \tag{4.22}$$

However, some simplifications can be made to avoid two-dimensional integration. For simplicity, we omit the fraction $\frac{1}{2\pi}$ and consider the case where x_{ij} is inside R. For x_{ij} on the border, the same method can be applied, with some simplifications. Therefore, consider the following integral, which, as can be seen, is equivalent to the previous one in the case where sigma is constant in the region.

$$\int_R \frac{\mathrm{Ki}_1(|x_{ij} - \mathbf{y}|_2)}{|x_{ij} - \mathbf{y}|_2} d\mathbf{y}. \tag{4.23}$$

Defining the polar coordinate system by taking $x_1 - y_1 = r\cos\theta$ and $x_2 - y_2 = r\sin\theta$, the area element becomes $d\mathbf{y} = rdrd\theta$. For an interior node, the medium is divided into four triangular regions, as shown in Figure 4.2. Then we can define the following trigonometric relations.

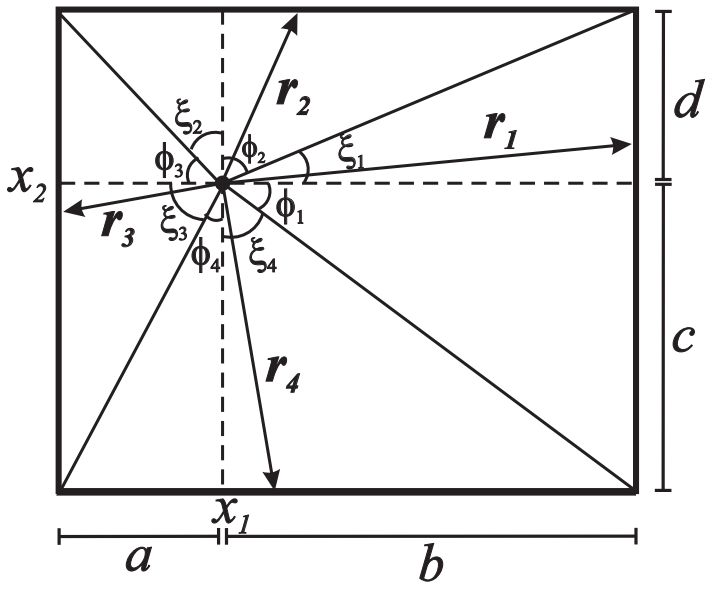

Figure 4.2: Schematic for polar integration.

$$\zeta_1 = \tan^{-1}\left(\frac{d}{b}\right) \qquad \phi_1 = \tan^{-1}\left(\frac{c}{b}\right) \qquad \rho_1 = \frac{b}{\cos\theta} \tag{4.24}$$

$$\zeta_2 = \tan^{-1}\left(\frac{a}{d}\right) \qquad \phi_2 = \tan^{-1}\left(\frac{b}{d}\right) \qquad \rho_2 = \frac{d}{\cos\theta} \tag{4.25}$$

$$\zeta_3 = \tan^{-1}\left(\frac{c}{a}\right) \qquad \phi_3 = \tan^{-1}\left(\frac{d}{a}\right) \qquad \rho_3 = \frac{a}{\cos\theta} \tag{4.26}$$

$$\zeta_4 = \tan^{-1}\left(\frac{b}{c}\right) \qquad \phi_4 = \tan^{-1}\left(\frac{a}{c}\right) \qquad \rho_4 = \frac{c}{\cos\theta} \tag{4.27}$$

Additionally, $\int_0^r \mathrm{Ki}_1(t)dt = \mathrm{Ki}_2(0) - \mathrm{Ki}_2(r)$. Thus,

$$\int_R \frac{\mathrm{Ki}_1(|x_{ij}-\mathbf{y}|_2)}{|x_{ij}-\mathbf{y}|_2} d\mathbf{y} = \sum_{k=1}^{4} \int_{-\phi_k}^{\zeta_k} \int_0^{\rho_k} \mathrm{Ki}_1(r) dr d\theta = \sum_{k=1}^{4} \int_{-\phi_k}^{\zeta_k} \left[\mathrm{Ki}_2(0) - \mathrm{Ki}_2(\rho_k)\right] d\theta \tag{4.28}$$

However, another change of variable can be applied to simplify this last integral. Thus, considering the case where $k = 1$, and using that $u = b\tan\theta$, $du = \frac{b}{\cos^2\theta} d\theta$, and $\cos^2\theta = \frac{b^2}{b^2+u^2}$, it is possible to write the first term of the sum of

Eq. (4.28), as

$$\int_{-\phi_1}^{\zeta_1} \left[\mathrm{Ki}_2(0) - \mathrm{Ki}_2(\rho_1)\right] d\theta = \int_{-\tan^{-1}\left(\frac{c}{b}\right)}^{\tan^{-1}\left(\frac{d}{b}\right)} \left[\mathrm{Ki}_2(0) - \mathrm{Ki}_2\left(\frac{b}{\cos\theta}\right)\right] d\theta \tag{4.29}$$

$$= \int_{-c}^{d} \left[\mathrm{Ki}_2(0) - \mathrm{Ki}_2\left(\sqrt{b^2+u^2}\right)\right] \frac{b}{b^2+u^2} du \tag{4.30}$$

Using the same methodology for the other terms, Eq. (4.28) can be expressed as

$$\int_R \frac{\mathrm{Ki}_1(|x_{ij}-\mathbf{y}|_2)}{|x_{ij}-\mathbf{y}|_2} d\mathbf{y} = \int_{-c}^{d} \left[\mathrm{Ki}_2(0) - \mathrm{Ki}_2\left(\sqrt{b^2+u^2}\right)\right] \frac{b}{b^2+u^2} du \tag{4.31}$$

$$+ \int_{-b}^{a} \left[\mathrm{Ki}_2(0) - \mathrm{Ki}_2\left(\sqrt{d^2+u^2}\right)\right] \frac{d}{d^2+u^2} du \tag{4.32}$$

$$+ \int_{-d}^{c} \left[\mathrm{Ki}_2(0) - \mathrm{Ki}_2\left(\sqrt{a^2+u^2}\right)\right] \frac{a}{a^2+u^2} du \tag{4.33}$$

$$+ \int_{-a}^{b} \left[\mathrm{Ki}_2(0) - \mathrm{Ki}_2\left(\sqrt{c^2+u^2}\right)\right] \frac{c}{c^2+u^2} du. \tag{4.34}$$

Although these changes may seem insignificant as they are just variable changes. Performance tests were carried out as a way to compare processing time before and after the changes. For this, tests were simulated with meshes of size $N \times N$, with N varying from 256 to 4096, over the region $[0,1] \times [0,1]$. The tests consisted of randomly choosing an $\mathbf{x}$ in R and calculating the integral form, Eq. (4.23), and the polar form, Eq. (4.31), for points on the previously specified mesh, those points are $\mathbf{y}$ values. Five simulations were carried out for each mesh size, and the average times for serial and parallel processing are presented in Table 4.1.

As can be seen, the use of parallelism in the code provided considerable time saving, reducing computational time by approximately 16 times when compared to serial implementation. Furthermore, when we compared the integral formulation with the polar formulation, 10 times better performance was observed, that is, a saving of 90% in processing time.

Furthermore, when we compare the integral formulation in serial and the polar formulation in parallel, we have a processing saving of around 165 times.

Table 4.1: Comparison of average processing time in seconds of serial and parallel calculation of K_{ij} using the integral and polar form.

$N \times N$	$N = 256$		$N = 512$		$N = 1024$		$N = 2048$		$N = 4096$	
	Se[a]	P[b]	Se	P	Se	P	Se	P	Se	P
Integral form - Eq. (4.23)	2.60	0.16	10.6	0.63	42.5	2.64	167.76	10.87	675.63	43.87
Polar form - Eq. (4.31)	0.26	0.01	0.96	0.06	3.85	0.25	15.5	1.07	65.1	4.08

[a] Serial implementation time.

[b] Parallel implementation time with OpenMP.

Therefore, it is safe to say that both the use of variable changes and parallelization are essential to obtain better computational time performance.

4.6 *Clipping distance* technique

Clipping, in the context of computer graphics, refers to removing the portion of the model that resides outside the horizontal and vertical bounds of the viewing area and outside the specified near and far depth bounds [25]. That is, clipping is a method to selectively enable or disable rendering operations within a defined region of interest. Mathematically, clipping can be described as a rendering algorithm that only draws pixels in the intersection between the clip region and the scene model, i.e., lines and surfaces outside the view volume are removed.

Clip regions are commonly specified to improve render performance. A well-chosen clip allows the renderer to save time by skipping calculations related to pixels that the user can not see. Pixels that will be drawn are said to be within the clip region. Pixels that will not be drawn are outside the clip region.

Here, the same idea was used to determine which regions interfere numerically with each other region. First, analyze the operator L_g presented in Eq. (3.16), which is defined by the integration of the kernel $k(\mathbf{x}, \mathbf{y})$ over the domain D, presented in Eq. (3.15). For a fixed value of $\mathbf{x}$, it is necessary to integrate the entire domain D, covering values of $\mathbf{y}$ in D. Thus, when performing numerical integration, the domain must be discretized into a numerical quadrature and the kernel must be calculated along this quadrature. So, for each value of $\mathbf{x}$ in this numerical quadrature, the $\mathbf{y}$ value must go through each of the mesh values.

However, as the kernel is dependent on the Ki_1 values and the distance between $\mathbf{x}$ and $\mathbf{y}$, if the ratio between these two is close to zero, then the contribution of this mesh point $\mathbf{y}$ to $\mathbf{x}$ is insignificant. In this way, when using the subregions technique, the domain D can be divided into $N_R \times N_R$ subregions, and thus individually evaluate the importance of each subregion. If the value of the kernel $k(\mathbf{x}, \mathbf{y})$ from $\mathbf{x}$ in a R_{ij} subregion to the vertices of the R_{kl} subregion is less than a specified tolerance, then the R_{kl} subregion is discarded and not computed throughout the code for the R_{ij} mesh.

Mathematically, we are expanding the integral between each subregion, i.e.,

$$(L_g f)(\mathbf{x}) = \int_D f(\mathbf{y})k(\mathbf{x}, \mathbf{y})d\mathbf{y} = \int_{R_{00}} f(\mathbf{y})k(\mathbf{x}, \mathbf{y})d\mathbf{y} + \int_{R_{01}} f(\mathbf{y})k(\mathbf{x}, \mathbf{y})d\mathbf{y} + \int_{R_{02}} f(\mathbf{y})k(\mathbf{x}, \mathbf{y})d\mathbf{y} + ... + \int_{R_{N_R N_R}} f(\mathbf{y})k(\mathbf{x}, \mathbf{y})d\mathbf{y} \tag{4.35}$$

and then, evaluating individually each kernel $k(\mathbf{x}, \mathbf{y})$ for each point $\mathbf{x}$.

As a way of verifying the effectiveness of using this technique, cases with two different tolerances and four different numbers of subregions were simulated. The tolerance, named *tol*, means that if $k(\mathbf{x}, \mathbf{y})$ is less than the tolerance, then the compared subregion will not be calculated when calculating $\mathbf{x}$ in the specific region.

In order to illustrate this process, figures for each of the situations were created. The region where $\mathbf{x}$ is, is highlighted in red, regions highlighted in gray are the ones removed from the calculation, i.e., do not affect the numerical result of the region in red, and the regions in white are the ones that were preserved. Such figures can be compared with Figure 3.2, which presents the reflection of the domain D. Therefore, there is a reflection of the domain on a central line both vertically and horizontally.

When considering $tol = 0$, we are considering all subregions as influential. This way, all subregions are painted white. However, when considering $tol = 10^{-1}$ and $tol = 10^{-2}$, we have a significant change in the influential regions, by increasing the number of subregions. Figure 4.3a to 4.4d illustrates these changes side-by-side.

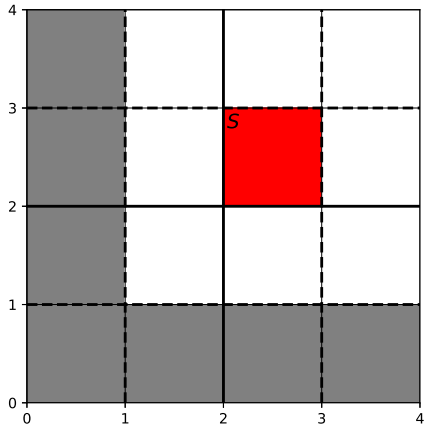

(a) $N_R = 1$, tolerance 10^{-1}

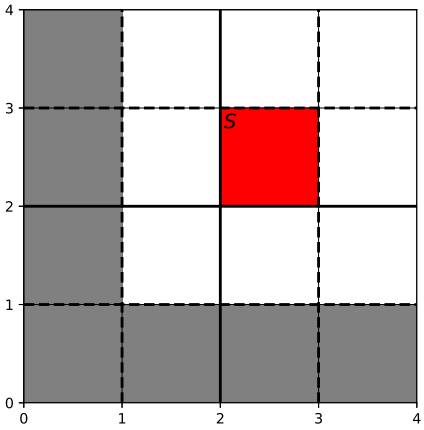

(b) $N_R = 1$, tolerance 10^{-2}

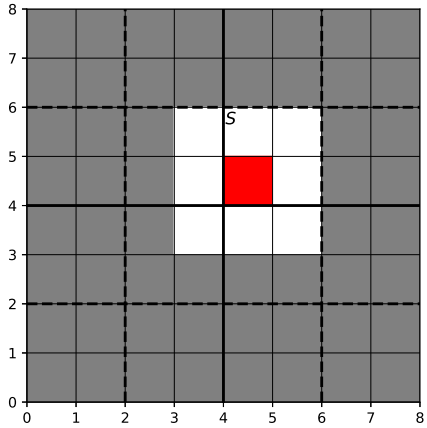

(c) $N_R = 2$, tolerance 10^{-1}

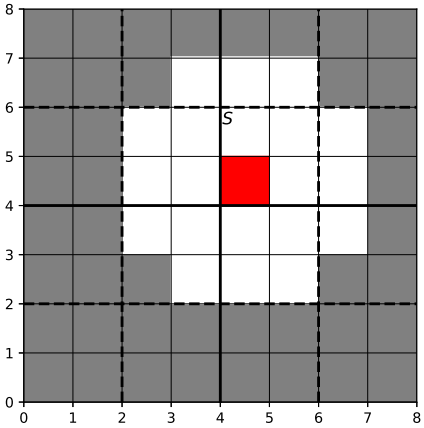

(d) $N_R = 2$, tolerance 10^{-2}

Figure 4.3: Clipping technique simulations, domain 10 cm by 10 cm, with different tolerance for $N_R = 1$ and 2.

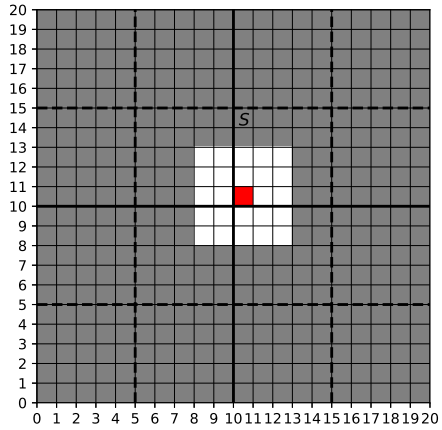

(a) $N_R = 5$, tolerance 10^{-1}

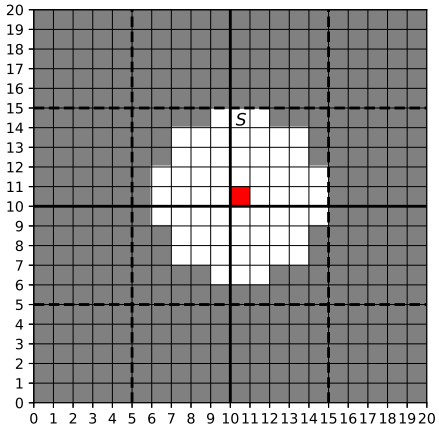

(b) $N_R = 5$, tolerance 10^{-2}

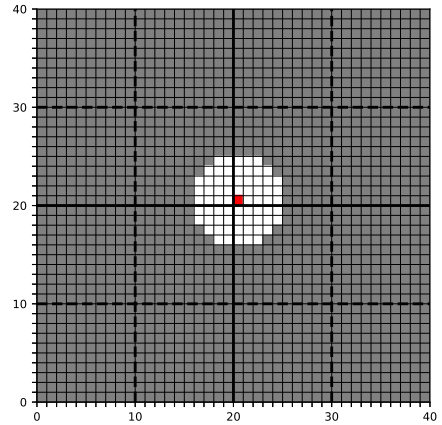

(c) $N_R = 10$, tolerance 10^{-1}

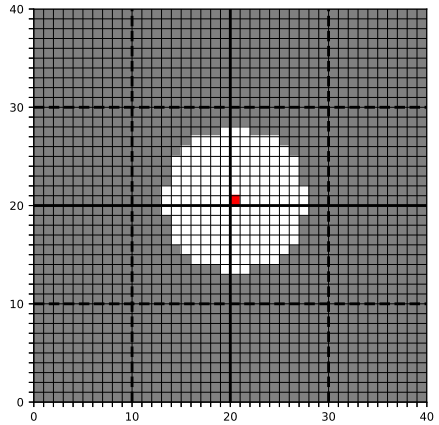

(d) $N_R = 10$, tolerance 10^{-2}

Figure 4.4: Clipping technique simulations, domain 10 cm by 10 cm, with different tolerance for $N_R = 5$ and 10.

As can be seen, although there is no difference when comparing domains with few subregions, Figures 4.3a and 4.3b, it is observed in Figures 4.3c and 4.3d that when increasing the number of subregions, a greater number of subregions is used to compute the numerical value of the cell in red. The same continues to occur, increasing the number of subregions even further, as seen in Figures 4.4a to 4.4d.

Thus, by increasing the number of subregions and decreasing tolerance, it is possible to cover a greater number of influential regions. On the other hand, the greater the number of influential regions calculated, the greater the processing time and computational effort.

Therefore, it is necessary to find a balance between both, seeking to eliminate the largest number of non-influential regions, but also preserving the numerical result, so as not to remove influential areas. A more in-depth discussion about the number of subregions and the tolerance will be done in Chapter 5 - Numerical Results, for each of the problems studied.

4.7 Implementation details

Although the algorithm essentially consists of calculating the sums in Eq. (4.14) using the iterative procedure with Eqs. (4.15a) and (4.15b), the techniques described previously were used to speed up the code and produce more accurate results. The following steps were considered:

1. Create $N_R \times N_R$ subregions over the domain D and assign for every subregion the corresponding values for σ_s, σ_t and S;

2. Assign a quadrature scheme to each subregion created in the previous item based on the input Δ and quadrature type selected, creating the submesh;

3. Calculate the clipping distance technique between the subregions and evaluate the tabulate necessity for each mesh. Excluding unnecessary subregions;

4. Tabulate K_{ij} and T^0_{ij}, Eqs. (4.16) and (4.15a), respectively, where the regions of integration are the squares defined in item 1 and the values of $\mathbf{x}$ are those defined in item 2;

5. Build and tabulate the terms of Neumann series, see Eq. (4.14), using the terms calculated in steps 1-4;

6. Compute the scalar flux at all points of the submeshes defined in item 2 with Eq. (4.14) using the previously tabulated items and the Rayleigh quotient, Eq. (4.17);

7. Compute the average scalar flux in each region and, if necessary, use the interpolation formula to calculate specific points outside the mesh grid.

The numerical results were produced by algorithms implemented in C++ 11.4, along with auxiliary libraries such as GSL Library - GNU Scientific Library Free Software Foundation 2.7.1 [54] and Cubature Library 1.0.3 [61].

GSL Library was mainly used to calculate the integrals for the change of variables, presented in Eq. 4.31. For that, the adaptive Gauss-Kronrod 21-point integration rule (*gsl_integration_qag*) was used, where the relative error limit was defined as 10^{-10}. This precision was chosen because it was possible to calculate the scalar flux with relative errors of the order of 10^{-9} or less.

Cubature Library is an adaptive multidimensional integration of vector-valued integrands via the Genz-Malik algorithm designed by the Ab-Initio Physics Research Group at the Massachusetts Institute of Technology. Cubature proved to be extremely efficient in integrations described in item 4 and has been routinely used by the research group due to its accuracy and computational efficiency.

OpenMP 5.2 [75] is an API (Application Programming Interface) that allows the distribution of activities to each of the threads of the same CPU in a

shared memory computer. So, the tasks were dynamically distributed among the threads. Thus, as soon as a thread finishes processing a job, it already receives another job so there is no idle thread. By doing so, we can make the most of the CPU we are using to calculate, and significantly reduce computational time.

This tool was used when calculating the distances between the meshes, item 3, which allowed each mesh to be distributed to a thread, which was in charge of checking the distance from the others and excluding sub-meshes that were not necessary. Furthermore, it was also possible to use parallelism during the tabulation of the terms presented in item 4. There are no dependencies between the terms and routines like Cubature and GSL integration can be parallelized, and thus obtain a significant time saving.

Additionally, OpenMP was used to minimize the computational running time spent on computing the terms of the Neumann Series, Eq. (4.14). This calculation was completely parallelized. The mesh could only be divided over the cores of a CPU because there is no dependence from any term of this iteration, just from the terms of the previous iteration, as can be noticed in Eq. (4.15b) where the term T^{n+1} depends only on T^n. Thus, for a given term n of the Neumann series, this vector was partitioned and distributed among the threads, so that they were all always busy. However, it is necessary to synchronize the threads in the vector end due to the need to use the n term of the series to calculate the $n+1$ term.

5 NUMERICAL RESULTS

This chapter presents the numerical results obtained using the methods and procedures described in the previous chapters for six problems already reported in the literature.

The first five problems studied here have a domain format similar to that shown in Figure 3.1, i.e., an internal source in the lower left corner, defining the region named R_1, followed by the other regions named R_2 to R_4, which have their sizes varying depending on the size of the domain and source. The last problem studied has a different geometry, having 4 regions, with three different properties. Its format will be presented later. Additionally, all problems consider the reflection only on the lower and left boundary. The upper and right borders are considered to be vacuum type.

The first two problems are test problems and aim to evaluate the effectiveness and performance of the method in homogeneous problems in a domain 1 cm by 1 cm. Problem 3 aims to evaluate the method in a larger domain, 10 cm by 10 cm, but in this case in a heterogeneous domain. This also allows us to check the code performance when dealing with a domain with different properties.

Problem 4, studies the case in a domain with even larger dimensions, 30 cm by 30 cm, but again a homogeneous case. The study of a problem with these characteristics aims to analyze the computational difficulties in calculations involving larger domains, which require a greater amount of mesh refinement, and a greater computational effort when compared to previous problems.

Problem 5 maintains the same structure as the previous case, but now in a heterogeneous domain. The idea of this case is to compare the effort required to go from a homogeneous case to a heterogeneous one. And if it is possible to

achieve the same numerical precision as in the previous problem, using the same refinements.

Finally, Problem 6 studies a case completely different from the others, with a domain 100 cm by 100 cm, divided into 4 regions with 3 of these having different properties. This allows us to analyze the performance for large domains, and the effectiveness of the method when dealing with problems in different characteristics and scattering and absorption with different orders of magnitude.

Furthermore, the number of subregions N_R is directly related to Δ because increasing the number of subregions reduces the size of each subregion, which reduces its quadrature, Eq. (4.1). Therefore, the values of Δ for each problem are directly linked to the size of the domain, and were chosen in order to build a mesh fine enough that convergence can be obtained, but also that it is possible to obtain the results in less than one hour. The more refined the mesh, the greater the number of points and the longer the processing time. Also, all problems were solved using the quadrature methodology presented in subsection 4.3 - *Numerical quadrature*.

The number of terms in the Neumann series was defined based on the change of the tenth decimal digit. If the terms of the series are changing the scalar flux by less than ten decimal places, the terms continue to be calculated. Otherwise, the series is considered to have converged, and the terms are no longer calculated.

All times presented here refer to wall time and were obtained by averaging the times of at least three repetitions. The computer used has an Intel Core i7 - 14700K 5.6 GHz processor (28 threads) and 32 GB of RAM DDR5 6000MHz, and to measure time, the function *omp_get_wtime* was used.

By convention, the result obtained considering tolerance 0 ($tol = 0$), i.e., not excluding any subregion, will be referred to as the solution to the problem.

This will be presented before the simulations with changes in tolerances, which will be compared with this solution using the relative error.

The units of measurement adopted are: the length of domain in cm, the internal source measured in $\mathrm{cm}^{-3}\mathrm{s}^{-1}$, Φ, σ_s, and σ_t are, respectively, $\mathrm{cm}^{-2}\mathrm{s}^{-1}$, cm^{-1}, and cm^{-1}.

5.1 Problem 1

This is a homogeneous problem that was set by Tsai and Loyalka [101], who studied it using integral methods. The domain is a square with unitary length, $a = b = 1$ cm, and a spatially constant square source of unit strength in the lower left corner with size 0.52 cm, i.e., $a_s = b_s = 0.52$ cm. Also, the total macroscopic cross section is 1.0 cm^{-1}, and several values for the scattering macroscopic cross sections were chosen according to those already presented in the literature.

This problem was also studied in several works such as Altaç and Spinrad [3] using SK_N, Altaç and Tekkalmaz [8] using $N - SK_N$ method, and Barichello *et al.* [19] using ADO method and Arbitrarily High Order Transport method (AHOT). However, they present numerical accuracy of only one or two decimal places or present the results in graphs, which makes numerical comparisons unfeasible.

For this problem, $\Delta = 10$ was chosen, and the number of subregions N_R ranged from 1 to 10. Also, 15 terms of the Neumann series were used for cases in which σ_s is less than 1, and 30 for the latter. The justification for this choice is that it was possible to generate results with the precision of two to three decimal places with only $N_R = 1$ and with a computational time of less than 0.2 seconds, for all cases, when compared at points.

Tables 5.1 - 5.5 list numerical results for the scalar flux evaluated at $x = y = 0.5$, $x = y = 0.7$ and $x = y = 0.98$, considering several values of σ_s, $tol = 0$, and compare it with the results presented by Tsai and Loyalka [101], Altaç and Spinrad [3] and Barichello [19]. Besides that, the results produced were compared with the code produced by Sauter *et al.* in [89]. This article studied two-dimensional problems in homogeneous domains with reflection in four boundaries of the square and presented good numerical precision.

Table 5.1: Comparison of the scalar flux at specific points and the average of flux in different locations of Problem 1 with $\Delta = 10$ and $tol = 0$, i.e., $a = b = 1.0$ cm, $a_s = b_s = 0.52$ cm, $\sigma_t = 1.0$ cm^{-1} and $\sigma_s = 0$ cm^{-1}.

Location	$N_R = 1$	$N_R = 2$	$N_R = 5$	$N_R = 10$	Tsai and Loyalka [101]	Altaç and Spinrad [3]	Sauter *et al.* [89]
$x = 0.5$	2.4271e-1	2.4271e-1	2.4271e-1	2.4271e-1	2.4271e-1	2.405e-1	2.4271e-1
$x = 0.7$	7.4228e-2	7.4228e-2	7.4228e-2	7.4228e-2	7.4296e-2	7.743e-2	7.4228e-2
$x = 0.98$	2.9367e-2	2.9367e-2	2.9367e-2	2.9367e-2	2.9371e-2	2.992e-2	2.9367e-2
R_1	4.4043e-1	4.3982e-1	4.3964e-1	4.3962e-1			4.2641e-1
R_2 and R_3	1.2837e-1	1.2865e-1	1.2873e-1	1.2875e-1			1.2718e-1
R_4	6.3333e-2	6.3329e-2	6.3328e-2	6.3328e-2			6.3531e-2

Note: $y = x$.

Table 5.2: Comparison of the scalar flux at specific points and the average of flux in different locations of Problem 1 with $\Delta = 10$ and $tol = 0$, i.e., $a = b = 1.0$ cm, $a_s = b_s = 0.52$ cm, $\sigma_t = 1.0$ cm^{-1} and $\sigma_s = 0.05$ cm^{-1}.

Location	$N_R = 1$	$N_R = 2$	$N_R = 5$	$N_R = 10$	Tsai and Loyalka [101]	Barichello *et al.* [19]	Sauter *et al.* [89]
$x = 0.5$	2.5067e-1	2.5046e-1	2.5038e-1	2.5042e-1	2.5053e-1	2.43e-1*	2.5044e-1
$x = 0.7$	7.8377e-2	7.8315e-2	7.8271e-2	7.8284e-2	7.8362e-2	7.8e-2*	7.8278e-2
$x = 0.98$	3.1012e-2	3.0937e-2	3.0952e-2	3.0937e-2	3.0931e-2	3.1e-2*	3.0924e-2
R_1	4.5275e-1	4.5214e-1	4.5197e-1	4.5195e-1			4.3837e-1
R_2 and R_3	1.3421e-1	1.3449e-1	1.3457e-1	1.3458e-1			1.3294e-1
R_4	6.6733e-2	6.6725e-2	6.6724e-2	6.6724e-2			6.6936e-2

the best result presented in the article. Note: $y = x$.

Table 5.3: Comparison of the scalar flux at specific points and the average of flux in different locations of Problem 1 with $\Delta = 10$ and $tol = 0$, i.e., $a = b = 1.0$ cm, $a_s = b_s = 0.52$ cm, $\sigma_t = 1.0$ cm^{-1} and $\sigma_s = 0.1$ cm^{-1}.

Location	$N_R = 1$	$N_R = 2$	$N_R = 5$	$N_R = 10$	Tsai and Loyalka [101]	Barichello *et al.* [19]	Sauter *et al.* [89]
$x = 0.5$	2.5919e-1	2.5877e-1	2.5860e-1	2.5868e-1	2.5891e-1	2.53e-1*	2.5872e-1
$x = 0.7$	8.2879e-2	8.2749e-2	8.2656e-2	8.2684e-2	8.2774e-2	8.1e-2*	8.2670e-2
$x = 0.98$	3.2799e-2	3.2639e-2	3.2671e-2	3.2639e-2	3.2622e-2	3.3e-2*	3.2612e-2
R_1	4.6586e-1	4.6525e-1	4.6508e-1	4.6506e-1			4.5108e-1
R_2 and R_3	1.4050e-1	1.4078e-1	1.4086e-1	1.4087e-1			1.3914e-1
R_4	7.0418e-2	7.0407e-2	7.0405e-2	7.0405e-2			7.0626e-2

the best result presented in the article. Note: $y = x$.

Table 5.4: Comparison of the scalar flux at specific points and the average of flux in different locations of Problem 1 with $\Delta = 10$ and $tol = 0$, i.e., $a = b = 1.0$ cm, $a_s = b_s = 0.52$ cm, $\sigma_t = 1.0$ cm^{-1} and $\sigma_s = 0.5$ cm^{-1}.

Location	$N_R = 1$	$N_R = 2$	$N_R = 5$	$N_R = 10$	Tsai and Loyalka [101]	Altaç and Spinrad [3]	Barichello *et al.* [19]	Sauter *et al.* [89]
$x = 0.5$	3.5773e-1	3.5507e-1	3.5391e-1	3.5441e-1	3.5589e-1	3.5761e-1	3.55e-1*	3.5469e-1
$x = 0.7$	1.3836e-1	1.3731e-1	1.3656e-1	1.3678e-1	1.3705e-1	1.4445e-1	1.32e-1*	1.3668e-1
$x = 0.98$	5.4919e-2	5.3575e-2	5.3840e-2	5.3578e-2	5.3413e-2	5.4950e-2	4.7e-2*	5.3357e-2
R_1	6.1166e-1	6.1113e-1	6.1097e-1	6.1095e-1				5.9255e-1
R_2 and R_3	2.1526e-1	2.1548e-1	2.1554e-1	2.1555e-1				2.1281e-1
R_4	1.1563e-1	1.1558e-1	1.1557e-1	1.1557e-1				1.1591e-1

* the best result presented in the article. Note: $y = x$.

Table 5.5: Comparison of the scalar flux at specific points and the average of flux in different locations of Problem 1 with $\Delta = 10$ and $tol = 0$, i.e., $a = b = 1.0$ cm, $a_s = b_s = 0.52$ cm, $\sigma_t = 1.0$ cm^{-1} and $\sigma_s = 1.0$ cm^{-1}.

Location	$N_R = 1$	$N_R = 2$	$N_R = 5$	$N_R = 10$	Tsai and Loyalka [101]	Altaç and Spinrad [3]	Sauter *et al.* [89]
$x = 0.5$	6.9354e-1	6.8451e-1	6.8024e-1	6.8197e-1	7.1530e-1	6.8741e-1	6.8305e-1
$x = 0.7$	3.5125e-1	3.4611e-1	3.4246e-1	3.4356e-1	3.7577e-1	3.4482e-1	3.4303e-1
$x = 0.98$	1.4065e-1	1.3373e-1	1.3507e-1	1.3374e-1	1.4692e-1	1.3302e-1	1.3264e-1
R_1	1.0672	1.0667	1.0665	1.0665			1.0344
R_2 and R_3	4.8224e-1	4.8225e-1	4.8226e-1	4.8227e-1			4.7588e-1
R_4	2.8782e-1	2.8761e-1	2.8756e-1	2.8755e-1			2.8829e-1

Note: $y = x$.

The results are in agreement with those presented by other papers in, at least, two decimal figures. In addition to the numerical results for some specific points, the tables present the average scalar flux in each of the regions of the domain. This data was not found in the literature.

As can be seen in the tables, the convergence is guaranteed regardless of σ_s values. It is also observed that when running the simplest problem, with $N_R = 1$, two to three decimal figurs of precision are obtained. Thus, bigger meshes are only needed when greater precision is desired.

Furthermore, the results are the same as those produced by the code of Sauter *et al.* [89], for the listed value of x. The difference occurs only when the average of each region is calculated. A justification for this is due to the fact that the mesh calculated using Sauter's code, 513 points, may not be fine enough to accurately calculate the average.

As a way to verify the efficiency of the clipping technique, new results were generated using 10^{-1} as tolerance. For values smaller than this, there were no effects as no mesh was removed. Therefore, Table 5.6 presents the largest relative error obtained among the average scalar flux in the regions when compared with the values presented in the Tables 5.1 - 5.5. The processing time for each case and the number of removed subregions, for multiple values of σ_s, N_R, and tol is also presented.

Table 5.6: Computational time, relative error and number of removed subregions for different σ_s, tolerances and number of subregions - Problem 1.

σ_s	tol		$N_R = 1$	$N_R = 2$	$N_R = 5$	$N_R = 10$
$\sigma_s = 0$ cm^{-1}	$tol = 0$	error	0	0	0	0
		time (s)	0.17	0.16	1.65	24.76
		removed	0	0	0	0
	$tol = 10^{-1}$	error	0	0	4.3298e-3	8.8709e-3
		time (s)	1.53	0.23	1.46	22.03
		removed	0	180	18088	351900
$\sigma_s = 0.05, 0.1,$ 0.5 cm^{-1}	$tol = 0$	error	0	0	0	0
		time (s)	0.16	0.54	11.97	377.13
		removed	0	0	0	0
	$tol = 10^{-1}$	error	0	2.2924e-3	9.8996e-3	1.5274e-2
		time (s)	0.09	0.33	8.17	334.98
		removed	0	180	18088	351900
$\sigma_s = 1.0$ cm^{-1}	$tol = 0$	error	0	0	0	0
		time (s)	0.17	1.62	18.87	767.07
		removed	0	0	0	0
	$tol = 10^{-1}$	error	0	5.7660e-3	1.9181e-2	2.6486e-2
		time (s)	0.16	1.79	15.78	671.72
		removed	0	180	18088	351900

As can be seen, when we compare the relative error for a fixed σ_s value, changing the tolerance, we have an error of the order of 10^{-3}. However, there is a gain in computational time, which varies from 12% to 14% for the largest meshes. It is worth mentioning that the number of removed subregions presented refers to the total number, not for a specific region. The gain is related to the high volume of subregions removed, more than 350 thousand meshes for the case $N_R = 10$.

In addition, notice that the processing time for the case with scattering cross section equal to one is always greater than the ones with smaller scattering. This is due to the fact that each of the terms of the series is always multiplied by the powers of σ_s, see Eq. (4.14). Thus, as the number of terms increases, the exponent increases, and the smaller the σ_s value is, the faster the series converges. However, when $\sigma_s = 1$ cm^{-1}, the coefficient does not decrease as the number of terms increases, thus, a greater number of terms are needed for convergence. This has a major impact on processing time, as the most time consuming process is the calculation of the terms of the Neumann series, which represents approximately 96% of the processing time for the largest meshes.

The contour lines shown in Figure 5.1 provide an insight into the distribution of the scalar flux across the domain. The Figures 5.1a and 5.1b present the flux for Problem 1 with $\sigma_s = 0.1$ cm^{-1} and $\sigma_s = 1$ cm^{-1}, respectively. As can be noticed, in both problems the further away from the source the lower the flux is. Besides that, note that the decrease is faster in the problem with $\sigma_s = 0.1$ cm^{-1} than with $\sigma_s = 1$ cm^{-1}, this is due to the fact that the scattering of particles is smaller in the first one than in the latter.

In addition, Figure 5.2 presents the value of the scalar flux in the diagonal of the domain for several values of σ_s. It is possible to observe an inflection in the flux when $x = 0.52$, because, from then on, the points are outside the source of the problem, and the flux is influenced only by the particles that leave it.

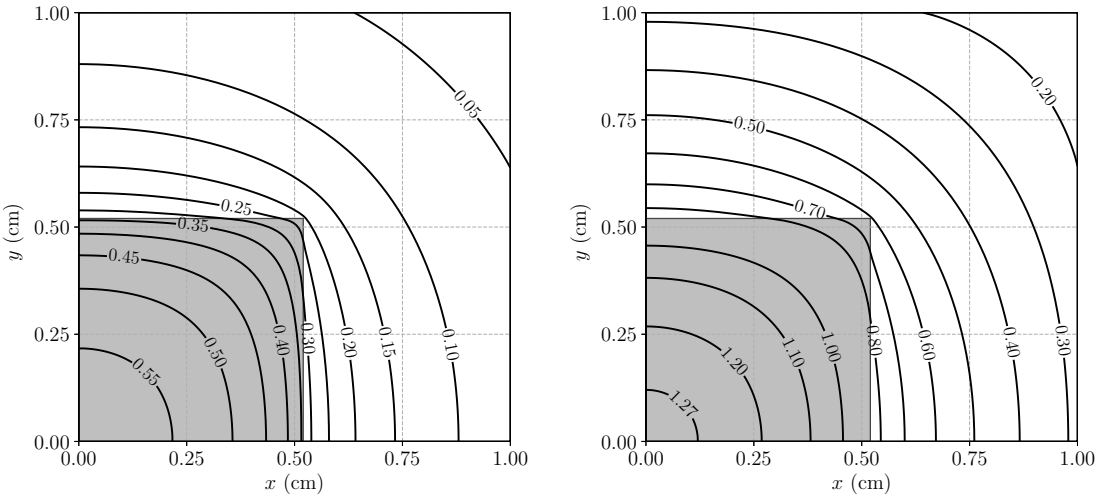

(a) $\sigma_s = 0.1$ cm^{-1} (b) $\sigma_s = 1$ cm^{-1}

Figure 5.1: Distribution of scalar flux along the domain for two cases of Problem 1: $a = b = 1.0$ cm, $a_s = b_s = 0.52$ cm, $\sigma_t = 1.0$ cm^{-1}.

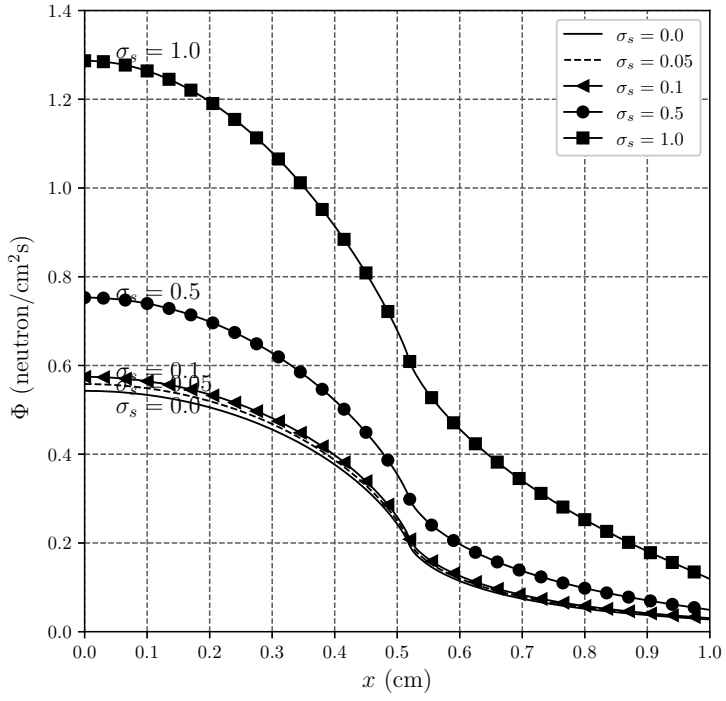

Figure 5.2: Scalar flux along the diagonal for different values of σ_s of Problem 1: $a = b = 1.0$ cm, $a_s = b_s = 0.52$ cm, $\sigma_t = 1.0$ cm^{-1} and $\sigma_s = 0$ to 1.0 cm^{-1}.

5.2 Problem 2

This problem has the same geometry as the previous one, but a smaller source. Therefore, this problem consists of a homogeneous square domain with sides $a = b = 1$ cm, with a source $S(x, y) = 1.0$ cm^{-3}s^{-1} in the region $[0, 0.5] \times [0, 0.5]$, i.e., $a_s = b_s = 0.5$ cm, and the total cross section is $\sigma_t = 1.0$ cm^{-1}. Also, it was considered the isotropic scattering case, where two values of the macroscopic scattering section were treated: in the first case $\sigma_s = 0.3$ cm^{-1}, and $\sigma_s = 0.9$ in the second case.

This problem was first proposed by Barichello *et al.* in [23], presenting results produced using the ADO and AHOT methods. However, some results were left out of this publication and were later presented in [21]. The latter, in addition to presenting new results, also reformulated the old ones giving more numerical precision.

In addition to these, Cromianski *et al.* [38], presented a study regarding the auxiliary equations that must be used in the ADO method in order to close the system and allow its solution. In such work, the authors proposed and analyzed approximations by constant, linear, and exponential functions. The results obtained are in agreement with those already presented by other nodal methods, in particular, those already presented in [21].

Tables 5.7 and 5.8 list numerical results for the average scalar flux in each of the regions of the domain, using $\Delta = 10$, N_R ranging from 1 to 10, and $tol = 0$.

Table 5.7: Comparison of the average scalar flux in each region of Problem 2: $a = b = 1.0$ cm, $a_s = b_s = 0.5$ cm, $\sigma_t = 1.0$ cm^{-1}, $\sigma_s = 0.3$ cm^{-1} and $\Delta = 10$, and $tol = 0$.

Region	$N_R = 1$	$N_R = 2$	$N_R = 5$	$N_R = 10$	Barichello *et al.* [23]	Barichello *et al.* [21]
R_1	5.1394e-1	5.1341e-1	5.1325e-1	5.1323e-1	5.1322e-1	5.1130e-1
R_2 and R_3	1.6270e-1	1.6297e-1	1.6305e-1	1.6306e-1		1.6345e-1
R_4	8.3828e-2	8.3805e-2	8.3800e-2	8.3800e-2		8.5345e-2

Table 5.8: Comparison of the average scalar flux in each region of Problem 2: $a = b = 1.0$ cm, $a_s = b_s = 0.5$ cm, $\sigma_t = 1.0$ cm^{-1}, $\sigma_s = 0.9$ cm^{-1} and $\Delta = 10$, and $tol = 0$.

Region	$N_R = 1$	$N_R = 2$	$N_R = 5$	$N_R = 10$	Barichello *et al.* [23]	Barichello *et al.* [21]
R_1	8.8943e-1	8.8901e-1	8.8887e-1	8.8885e-1	8.8661e-1	8.8766e-1
R_2 and R_3	3.7365e-1	3.7379e-1	3.7384e-1	3.7385e-1	3.7360e-1	3.7391e-1
R_4	2.1775e-1	2.1762e-1	2.1759e-1	2.1758e-1	2.1887e-1	2.1904e-1

Note that the numerical results are in agreement with those already reported in other works by, at least, two significant figures. Furthermore, the results show a smooth convergence, and with the finest mesh, it is possible to obtain 2 to 3 digits of precision.

To evaluate the effectiveness of the clipping method, experiments were conducted with a tolerance set at 10^{-1}. In cases where values are smaller than this, no change was observed as no subregions were eliminated. Table 5.9 displays the maximum relative error observed across all regions in comparison to the data listed in the previous tables, Tables 5.7 and 5.8. Also, the computational time for each

case and the number of removed subregions, considering different settings for σ_s, N_R, and tol are presented.

Table 5.9: Computational time, relative error and number of removed subregions for different σ_s, tolerances and number of subregions - Problem 2.

σ_s	tol		$N_R = 1$	$N_R = 2$	$N_R = 5$	$N_R = 10$
$\sigma_s = 0.3$ cm^{-1}	$tol = 0$	error	0	0	0	0
		time (s)	0.14	0.33	6.88	248.83
		removed	0	0	0	0
	$tol = 10^{-1}$	error	0	1.1119e-3	5.4337e-3	1.0855e-2
		time (s)	0.10	0.30	6.24	226.87
		removed	0	140	16192	330232
$\sigma_s = 0.9$ cm^{-1}	$tol = 0$	error	0	0	0	0
		time (s)	0.18	0.43	16.07	630.76
		removed	0	0	0	0
	$tol = 10^{-1}$	error	0	4.2125e-3	1.4305e-2	2.2078e-2
		time (s)	0.17	0.39	12.95	559.40
		removed	0	140	16192	330232

As mentioned previously, even with the use of coarse meshes such as $N_R = 1$ and $N_R = 2$, it is already possible to obtain 2 to 3 digits of precision, in a short time, less than a second, as shown in Table 5.6. Once again we can see a gain in computational time when removing unnecessary subregions, gaining 9% to 12% of processing time.

However, as analyzed previously, the convergence of the Neumann series for the second case is slower because σ_s is close to 1 cm^{-1}. Thus, 25 terms of the series were needed for the second case, while for the first case, only 15 terms were sufficient.

5.3 Problem 3

The first heterogeneous media problem analyzed here was proposed by Azmy [15] and later studied by Mello and Barros [42] and Barichello *et al.* [20, 21]. The geometry follows the same as the previous case, except that for this problem we consider a larger internal domain and source, being: $a = b = 10.0$ cm, and $a_s = b_s = 5.0$ cm and the source $S(x, y) = 1.0$ cm^{-3}s^{-1} is located in section R_1. Continuing in the source section, $\sigma_t = 1.0$ cm^{-1} and $\sigma_s = 0.5$ cm^{-1}, while for all other regions, R_2 to R_4, $\sigma_t = 2.0$ cm^{-1} and $\sigma_s = 0.1$ cm^{-1}.

The average scalar flux for this problem with $\Delta = 2$ and $tol = 0$ is presented in Table 5.10. The results presented in the literature were produced by already consolidated methods, such as LN by Azmy [15], Mello and Barros [42] used the SGF-ExpN method and Barichello *et al.* [20, 21] used ADO-Nodal method.

Table 5.10: Average scalar flux for each region with $\Delta = 2$ in Problem 3: $a = b = 10.0$ cm, $a_s = b_s = 5.0$ cm, $\sigma_t = 1.0$ cm^{-1} and $\sigma_s = 0.5$ cm^{-1} in R_1 while for all other regions, $\sigma_t = 2.0$ cm^{-1} and $\sigma_s = 0.1$ cm^{-1}.

Region	$N_R = 1$	$N_R = 2$	$N_R = 5$	$N_R = 10$	Azmy [15]	Mello and Barros [42]	Barrichello *et al.* [21]
R_1	1.6879	1.6877	1.6853	1.6851	1.676	1.676	1.6840
R_2 and R_3	4.0049e-2	4.0050e-2	4.0176e-2	4.0465e-2	4.159e-2	4.161e-2	4.0663e-2
R_4	1.8033e-3	1.8032e-3	1.7773e-3	1.7739e-3	1.992e-3	1.993e-3	1.8259e-3

It can be observed that the results produced for R_1,R_2 and R_3 are in agreement with those already presented by the authors and are converging as the number of subregions increases. Also, note that by choosing $N_R = 1$ it is already possible to ensure two to three decimal places of precision for three regions, with a low computational cost.

Table 5.11 displays the maximum relative error observed across all regions in comparison to the data listed in the previous table, Table 5.10. Also, the computational time for each case and the number of removed subregions, considering different settings for N_R and tol are presented.

Table 5.11: Computational time, relative error and number of removed subregions for different tolerances and number of subregions - Problem 3.

tol		$N_R = 1$	$N_R = 2$	$N_R = 5$	$N_R = 10$
	error	0	0	0	0
$tol = 0$	time (s)	1.26	1.95	15.55	453.58
	removed	0	0	0	0
	error	3.6276e-3	7.9499e-2	2.9972e-1	4.6609e-1
$tol = 10^{-1}$	time (s)	0.45	0.43	0.81	10.00
	removed	156	3612	154916	2505188
	error	3.6276e-3	4.8510e-2	1.0581e-1	1.9247e-1
$tol = 10^{-2}$	time (s)	0.47	0.41	3.18	16.50
	removed	156	3404	147692	2431804
	error	3.6276e-3	1.2132e-2	2.8782e-2	5.8358e-2
$tol = 10^{-3}$	time (s)	0.46	2.72	1.81	31.68
	removed	156	3308	139356	2321792
	error	1.8599e-3	1.5138e-3	6.9700e-3	1.3331e-2
$tol = 10^{-4}$	time (s)	0.78	0.72	5.01	43.88
	removed	100	2744	128020	2157184
	error	1.6636e-7	9.8824e-5	1.2788e-3	2.6552e-3
$tol = 10^{-5}$	time (s)	0.67	1.09	3.11	64.92
	removed	68	2260	114988	1970856

As reported in previous cases, the removal of subregions that reach a specific minimum tolerance has resulted in a significant gain in computational time.

When comparing the processing time, for the case for $N_R = 10$ when no removal is made, $tol = 0$, and the case with $tol = 10^{-1}$, it is possible to reduce the processing time by 98%, going from 453 seconds to 10 seconds. This time reduction is due to the removal of more than 2.5 million subregions considered unnecessary.

However, a relative error of 4.66×10^{-1} is observed, and an absolute error of the order of 0.12. Thus, although there is a gain in processing time, there is a loss in the numerical result for the scalar flux. This is due to the fact that a large number of meshes with low importance are being removed, which causes spurious errors.

The same event can be observed when comparing the results of non-removal meshes with the ones with $tol = 10^{-2}$. This presents a significant time reduction of 96%, but a relative error of 1.9×10^{-1} and an absolute error of 0.02, which is considered significant. However, when considering an even lower tolerance, both errors decrease drastically, presenting numerical differences only in the third decimal place, with 93% less time processing for $tol = 10^{-3}$.

Thus, we can observe that an increase in the number of removed subregions, although it seems beneficial for reducing time, has as a counterpoint a larger numerical error in the scalar flux. On the other hand, using a smaller tolerance, for example, $tol = 10^{-5}$, has a gain in precision, but also an increase in time.

Therefore, the choice of tolerance used is extremely important for the search for quick and accurate results. In this case, it is considered that using $tol = 10^{-3}$ is more advantageous than the others. Since increasing it presents larger errors, and decreasing it presents a greater computing time, and an accuracy not proportional to the time spent.

As a way to check the numerical accuracy when increasing the Δ value, a new problem was simulated with $\Delta = 10$. The results for this case are presented in Table 5.12, as well as with its computational time.

Table 5.12: Average scalar flux and processing time for each region with $\Delta = 10$ in Problem 3: $a = b = 10.0$ cm, $a_s = b_s = 5.0$ cm, $\sigma_t = 1.0$ cm^{-1} and $\sigma_s = 0.5$ cm^{-1} in R_1 while for all other regions, $\sigma_t = 2.0$ cm^{-1} and $\sigma_s = 0.1$ cm^{-1}.

Region	$N_R = 1$	$N_R = 2$	$N_R = 5$	$N_R = 10$	Azmy [15]	Mello and Barros [42]	Barrichello *et al.* [21]
R_1	1.6851	1.6851	1.6851	1.6851	1.676	1.676	1.6840
R_2 and R_3	4.0538e-2	4.0543e-2	4.0544e-2	4.0544e-2	4.159e-2	4.161e-2	4.0663e-2
R_4	1.7738e-3	1.7738e-3	1.7738e-3	1.7738e-3	1.992e-3	1.993e-3	1.8259e-3
time (s)	475	716	1474	3086			

As can be seen when comparing Tables 5.12 with Tables 5.10 and 5.11. When using $\Delta = 10$, we have a high refinement of the mesh, which implies an increase in computational time, almost 7 times more. However, a greater numerical precision was not observed, as the greater refinement presented the same numerical result. Thus, it is observed that increasing the mesh size with the intention of obtaining better results may not always be a good strategy, since the gain in precision sometimes does not outweigh the increase in processing time.

Also, due to the scalar flux being close to zero in the region R_4, catastrophic cancellations may be happening which makes it extremely difficult to accurately compute exact values in that region. As can be seen in Figure 5.3, as well as physically expected, the further away from the source, the smaller the scalar flux. In addition, note that the decay in the flux close to the source is relatively large, thus, along the domain, a large number of points has a very small flux and numerical handling becomes complicated.

Figure 5.3 provides insight into the distribution of scalar flux across the domain. Note that the flux distribution within the region R_1, where the internal source is located, slowly decreases. As can be seen, close to the edge of the source, the flux is equal to 1.0 neutron.cm^{-2}s^{-1}. However, just a few millimeters to the right there is a sharp decay in a short distance, as it can be observed that the flux drops to 0.5 neutron.cm^{-2}s^{-1} on the outside of the source and faster to 0.2 neutron.cm^{-2}s^{-1}.

Nonetheless, note that the flux in the regions R_2, R_3 and R_4 assume values close to zero, so any change in a point can cause noise in the average of the region. Thus, precision in integrations and tabulations must be taken into account for this type of problem.

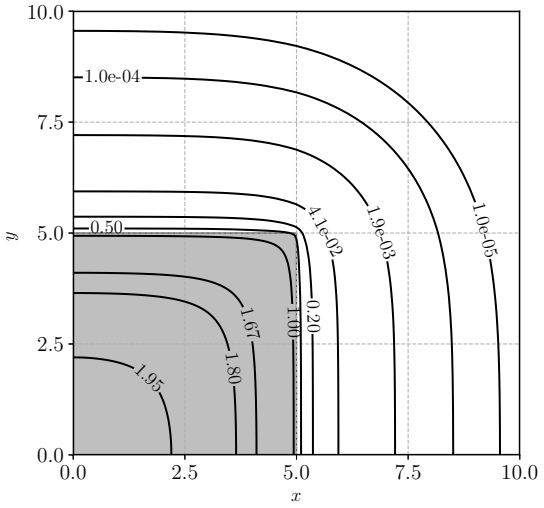

Figure 5.3: Contour lines of the scalar flux for Problem 3: $a = b = 10.0$ cm, $a_s = b_s = 5.0$ cm, $\sigma_t = 1.0$ cm^{-1} and $\sigma_s = 0.5$ cm^{-1} in R_1 while for all other regions, $\sigma_t = 2.0$ cm^{-1} and $\sigma_s = 0.1$ cm^{-1}.

5.4 Problem 4

This problem has the same characteristics as Problem 2, but a new configuration of the domain structure. The idea of analyzing this problem comes from the fact that it makes it possible to evaluate the effectiveness of the clipping technique on a larger and homogeneous domain.

This problem consists of a homogeneous square domain with sides $a = b = 30$ cm, with a small source $S(x, y) = 1.0$ cm^{-3}s^{-1} in the region $[0, 10] \times [0, 10]$ ($a_s = b_s = 10$ cm), and the total cross section is $\sigma_t = 1.0$ cm^{-1}. Also, it was considered the isotropic scattering case, where two values of the macroscopic scattering

section were treated: in the first case $\sigma_s = 0.3$ cm^{-1}, and $\sigma_s = 0.9$ in the second case.

This problem was proposed by Cromianski *et al.* in [38]. As previously presented, in such work the ADO method was used and approximations of transverse leakage terms by constant, linear, and exponential functions were proposed and analyzed as a way to complete the linear system of the method. However, the averages for some regions for the case $\sigma_s = 0.3$ cm^{-1} were not presented in the work and it was not possible to find any reference in the literature.

Tables 5.13 and 5.14 list the numerical results for the average scalar flux in each of the regions of the domain, using $\Delta = 2$, $tol = 0$, and N_R ranging from 1 to 10 and for $\sigma_s = 0.3$ cm^{-1} and $\sigma_s = 0.9$ cm^{-1}, respectively.

Table 5.13: Average scalar flux for each region with $\Delta = 2$ in Problem 4: $a = b =$ 30.0 cm, $a_s = b_s = 10.0$ cm, $\sigma_t = 1.0$ cm^{-1} and $\sigma_s = 0.3$ cm^{-1}.

Region	$N_R = 1$	$N_R = 2$	$N_R = 5$	$N_R = 10$	Cromianski *et al.* [38]
R_1	1.3435	1.3435	1.3432	1.3428	1.3420
R_2 and R_3	2.0708e-2	2.0707e-2	2.0778e-2	2.0733e-2	
R_4	5.4338e-4	5.4339e-4	5.4242e-4	5.4134e-4	

Table 5.14: Average scalar flux for each region with $\Delta = 2$ in Problem 4: $a = b =$ 30.0 cm, $a_s = b_s = 10.0$ cm, $\sigma_t = 1.0$ cm^{-1} and $\sigma_s = 0.9$ cm^{-1}.

Region	$N_R = 1$	$N_R = 2$	$N_R = 5$	$N_R = 10$	Cromianski *et al.* [38]
R_1	8.3294	8.3260	8.3210	8.3242	8.3160
R_2 and R_3	3.9030e-1	3.9015e-1	3.9025e-1	3.9052e-1	3.9400e-1
R_4	2.6319e-2	2.6319e-2	2.6375e-2	2.6410e-2	2.6920e-2

As can be seen, for the first case, using $N_R = 1$, it is already possible to obtain a 2-digit approximation to the values presented by Cromianski *et al* [38] in R_1. Unfortunately, the values for the other regions were not found in the literature.

The same happens for the second case, in which we have a convergence of the values presented. As well as a difference only in the third significant digit with the values presented in the literature.

Table 5.15 presents the values of computational time, relative error when compared with the values presented in previous tables, and the number of meshes removed.

As presented in Problem 3, it is observed that the exaggerated removal of subregions causes strong numerical imperfections in the scalar flux. For the first case, with $\sigma_s = 0.3$ cm^{-1}, comparing the largest of the meshes, for the case of $tol = 0$ and $tol = 10^{-1}$, the absolute error between them is of the order of 0.06, with a reduction of 97% in processing time. When analyzing the same situation, but for $\sigma = 0.9$ cm^{-1}, a reduction from 3065 seconds to approximately 15 seconds is observed, a reduction of more than 200 times. However, the numerical error here for the average scalar flux is from the correct 8.324 to 6.284. This last value does not match the reality of the problem. So, obviously, necessary meshes are being removed inappropriately. The same happens by reducing the tolerance to $tol = 10^{-2}$, numerical results far from the reality of the problem are being obtained.

Thus, once again the use of tolerances of the order of $tol = 10^{-3}$ and $tol = 10^{-4}$ are more recommended for problems in larger domains. It is also observed that the difference in computational time for these tolerances is more than 20 times less than the time without removal. This is because more than 2 million non-influential subregions are being removed, and even so, obtaining numerical precision and expected scalar flux for the problem.

Table 5.15: Computational time, relative error and number of removed subregions for different σ_s, tolerances and number of subregions - Problem 4.

σ_s	tol		$N_R = 1$	$N_R = 2$	$N_R = 5$	$N_R = 10$
$\sigma_s = 0.3$ cm^{-1}	$tol = 0$	error	0	0	0	0
		time (s)	5.45	9.46	46.99	383.05
		removed	0	0	0	0
	$tol = 10^{-1}$	error	4.3947e-5	8.1848e-3	2.0959e-1	3.3761e-1
		time (s)	1.39	0.96	1.28	9.09
		removed	156	3612	156636	2535036
	$tol = 10^{-2}$	error	4.3947e-5	8.1848e-3	4.5750e-2	1.0342e-1
		time (s)	1.37	0.94	1.486	10.86
		removed	156	3612	153916	2496736
	$tol = 10^{-3}$	error	4.3947e-5	8.1848e-3	7.9481e-3	3.0917e-2
		time (s)	1.37	0.99	2.19	12.69
		removed	156	3612	148612	2453536
	$tol = 10^{-4}$	error	4.3947e-5	2.2500e-4	1.7987e-3	6.2956e-3
		time (s)	1.47	1.20	2.55	15.82
		removed	156	3260	144336	2385052
$\sigma_s = 0.9$ cm^{-1}	$tol = 0$	error	0	0	0	0
		time (s)	43.22	69.08	374.61	3065
		removed	0	0	0	0
	$tol = 10^{-1}$	error	4.4607e-5	1.0361e-2	3.5627e-1	5.8107e-1
		time (s)	10.24	4.33	3.50	15.36
		removed	156	3612	156636	2535036
	$tol = 10^{-2}$	error	4.4607e-5	1.0361e-2	7.1633e-2	1.5782e-1
		time (s)	8.75	4.35	4.94	25.68
		removed	156	3612	153916	2496736
	$tol = 10^{-3}$	error	4.4607e-5	1.0361e-2	1.0511e-2	4.5682e-2
		time (s)	8.95	4.52	10.58	38.62
		removed	156	3612	148612	2453536
	$tol = 10^{-4}$	error	4.4607e-5	1.8990e-4	2.1174e-3	8.1779e-3
		time (s)	9.15	6.64	12.70	62.56
		removed	156	3260	144336	2385052

Again, the difference in processing time, for cases with different σ_s, is due to the number of terms in the Neumann series. As explained previously, the closer σ_s is to 1, the more terms in the series are needed. For this problem, only 15 terms were needed for the first case, and 120 terms for the second case. Such quantities were necessary to ensure convergence of at least 6 decimal places.

Therefore, processing the terms in the series proved to be costly in computational time. Table 5.16 presents the time to calculate each of the terms of the Neumann series for each of σ_s, varying the number of subregions, for $tol = 0$.

Table 5.16: Average CPU time for Problem 4 and for each term of the Neumann series increasing the number of subregions, for $tol = 0$.

σ_s	$N_R = 1$	$N_R = 2$	$N_R = 5$	$N_R = 10$
0.3	5 s	9 s	45 s	366 s
0.9	42 s	68 s	370 s	3040 s
Time each term of the Neumann series	0.3 s	0.5 s	3 s	25.5 s

As can be seen, the calculation of all terms in the Neumann series takes up to 95% to 99% of the total time, without removing the meshes. Removing those subregions, several unnecessary regions are eliminated, and thus the total time is drastically reduced, as presented in Table 5.15.

5.5 Problem 5

Problem 5 mixes features of the last two problems, inheriting the physical properties of Problem 3 and the size of the domain and source of Problem 4. Therefore, $a = b = 30.0$ cm, and $a_s = b_s = 10.0$ cm. As before, the source $S(x, y) = 1.0$ cm^{-3}s^{-1} is located in section R_1. Continuing in the source section,

$\sigma_t = 1.0$ cm^{-1} and $\sigma_s = 0.5$ cm^{-1}, while for all regions R_2 to R_4, $\sigma_t = 2.0$ cm^{-1} and $\sigma_s = 0.1$ cm^{-1}.

This problem was proposed by Barichello *et al.* in [21] who studied it using the ADO-Nodal and AHOT-N0 methods. In this work, at least two decimal places of convergence were observed.

Table 5.17 presents the average scalar flux for each of the regions using $\Delta = 2$, $tol = 0$, and 18 Neumann series terms were used to ensure convergence.

Table 5.17: Average scalar flux for each region with $\Delta = 2$ in Problem 5: $a = b = 30.0$ cm, $a_s = b_s = 10.0$ cm, $\sigma_t = 1.0$ cm^{-1} and $\sigma_s = 0.5$ cm^{-1} in R_1 while for all other regions, $\sigma_t = 2.0$ cm^{-1} and $\sigma_s = 0.1$ cm^{-1}.

Region	$N_R = 1$	$N_R = 2$	$N_R = 5$	$N_R = 10$	Barichello *et al.* [21] ADO-Nodal	Barichello *et al.* [21] AHOT-N0
R_1	1.8381	1.8380	1.8374	1.8368	1.8362	1.8360
R_2 and R_3	1.0500e-2	1.0503e-2	1.0461e-2	1.0536e-2	1.0658e-2	1.0678e-2
R_4	1.1272e-4	1.1272e-4	1.1201e-4	1.1110e-4	1.1739e-4	1.1258e-4

It can be observed that the results produced are in agreement with those already presented by the authors and are converging as the number of subregions increases. Also, note that by choosing $N_R = 1$ it is already possible to ensure two significant digits of precision with a low computational cost.

Table 5.18 presents the values of computational time, relative error when compared with the values presented in previous tables, and the number of meshes removed.

This problem, as well as the others previously described, using a tolerance of the order of 10^{-1}, presented numerical imperfections. However, for this problem, a smaller relative error was observed when using $tol = 10^{-2}$ that was observed in other problems. When using $tol = 10^{-2}$ it was possible to obtain an absolute error for the scalar flux of the order of 0.01, compared with $tol = 0$ and

Table 5.18: Computational time, relative error and number of removed subregions for different tolerances and number of subregions - Problem 5.

tol		$N_R = 1$	$N_R = 2$	$N_R = 5$	$N_R = 10$
	error	0	0	0	0
$tol = 0$	time (s)	90.77	134.35	327.03	1699.18
	removed	0	0	0	0
	error	1.2597e-5	3.6702e-3	1.3376e-1	1.6002e-1
$tol = 10^{-1}$	time (s)	18.34	9.33	6.02	14.50
	removed	156	3612	156636	2539436
	error	1.2597e-5	3.6702e-3	1.2872e-2	5.9933e-2
$tol = 10^{-2}$	time (s)	17.60	10.97	5.36	18.36
	removed	156	3612	154916	2521372
	error	1.2597e-5	3.6702e-3	2.1323e-3	1.5920e-2
$tol = 10^{-3}$	time (s)	18.37	10.39	7.34	21.23
	removed	156	3612	152008	2489172
	error	1.2597e-5	1.8818e-3	6.9558e-4	3.3387e-3
$tol = 10^{-4}$	time (s)	18.69	12.28	6.50	31.01
	removed	156	3404	149988	2453220
	error	1.2597e-5	1.2775e-5	1.6802e-4	6.1046e-4
$tol = 10^{-5}$	time (s)	17.30	10.91	8.74	30.78
	removed	156	3308	145172	2405748

$N_R = 10$. For instance, this error is smaller than that described in Problems 2 and 4, which were 0.02 and 0.39, respectively.

In addition, Figure 5.4 provides the scalar flux distribution across the domain. Note that the average flux is very small for the regions outside the source and that the decay of the flux outside of the source is extremely fast. So, any error in the scalar flux of some points and catastrophic cancellations can cause numerical noise in the average.

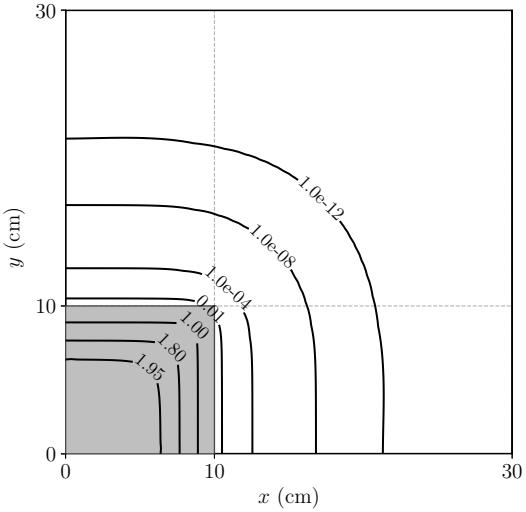

Figure 5.4: Contour lines of the scalar flux for Problem 5: $a = b = 30.0$ cm, $a_s = b_s = 10.0$ cm, $\sigma_t = 1.0$ cm^{-1} and $\sigma_s = 0.5$ cm^{-1} in R_1 while for all other regions, $\sigma_t = 2.0$ cm^{-1} and $\sigma_s = 0.1$ cm^{-1}.

5.6 Problem 6

Problem 6 has a different geometry than those previously studied. This has an even larger domain, 100 cm by 100 cm, with an internal source, measuring 40 cm by 40 cm, and is surrounded by 3 regions with different properties. This problem aims to study the effectiveness of the method described here, for even more complex problems. The geometry of this problem is presented in Figure 5.5.

Such problem was proposed by Azmy [17] as an heterogeneous square medium, $a = b = 100.0$ cm, where the unity source $S(x, y) = 1.0$ cm^{-3}s^{-1} is located in section R_1, $a_s = b_s = 40.0$. The following physical parameters are associated with each one of the regions in: section R_1: $\sigma_t = 1$ cm^{-1}, $\sigma_s = 0.5$ cm^{-1}; section R_2: $\sigma_t = 0.1$ cm^{-1}, $\sigma_s = 0.01$ cm^{-1}; section R_3: $\sigma_t = 0.3$ cm^{-1}, $\sigma_s = 0.1$ cm^{-1}, and section R_4: $\sigma_t = 0.1$ cm^{-1}, $\sigma_s = 0.01$ cm^{-1}.

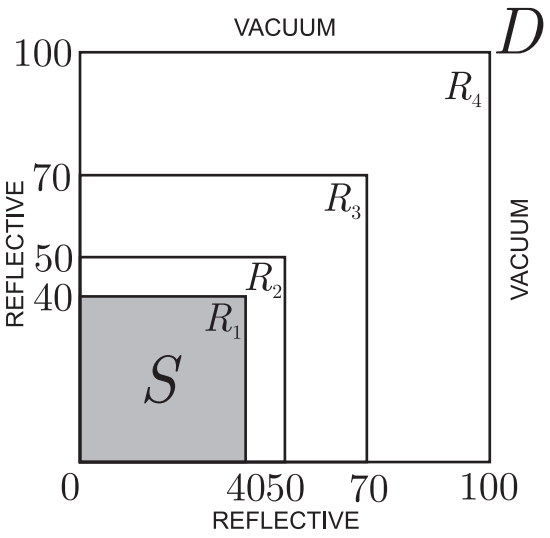

Figure 5.5: Two-dimensional geometry of the test Problem 6.

This problem was studied by Azmy [17], using the LN method, and more recently by Barichello *et al.* [21], using ADO-Nodal and AHOT-N0 methods.

Table 5.19 presents the average scalar flux for each of the regions using $\Delta = 2$, $tol = 0$, and 40 Neumann series terms to ensure convergence.

It is evident that the obtained results align with those previously reported by the authors and exhibit convergence as the number of subregions increases. Notably, opting for $N_R = 1$ it is already possible to ensure three decimal places of precision at R_1 and two digit in other regions with a low computational cost.

Table 5.19: Average scalar flux for each region with $\Delta = 2$ in Problem 6: $a = b = 100.0$ cm, $S(x, y) = 1.0$ is in section R_1, $a_s = b_s = 40.0$. Section R_1: $\sigma_t = 1$ cm^{-1}, $\sigma_s = 0.5$ cm^{-1}; section R_2: $\sigma_t = 0.1$ cm^{-1}, $\sigma_s = 0.01$ cm^{-1}; section R_3: $\sigma_t = 0.3$ cm^{-1}, $\sigma_s = 0.1$ cm^{-1}, and section R_4: $\sigma_t = 0.1$ cm^{-1}, $\sigma_s = 0.01$ cm^{-1}.

Region	$N_R = 1$	$N_R = 2$	$N_R = 5$	$N_R = 10$	Azmy [17]	Barichello *et al.* [21]
R_1	1.9589	1.9587	1.9589	1.9586	1.957	1.9584
R_2	3.1543e-1	3.1670e-1	3.1756e-1	3.1742e-1	3.339e-1	3.1833e-1
R_3	1.5720e-2	1.5721e-2	1.5713e-2	1.5699e-2	1.504e-2	1.5585e-2
R_4	2.6469e-5	2.6557e-5	2.6655e-5	2.6636e-5	2.682e-5	2.6507e-5

Table 5.18 illustrates the computational time, relative error concerning values from earlier tables, and the count of eliminated meshes.

Note that not using the clipping technique, i.e., using $tol = 0$, results in an extremely high computational cost when compared to the previous problem. Problem 6, with $N_R = 10$, required approximately 11 hours of processing, while the previous problem required less than 30 minutes. That is, this problem is more than 20 times more computationally expensive than the previous problem.

Similar to the preceding scenarios, employing a tolerance of 10^{-1} resulted in a significant decrease in processing time. When we compared the most refined mesh $N_R = 10$, the processing time was reduced by 65 times, from 11 hours to approximately 10 minutes. All of this is due to the fact that more than 58 million unnecessary subregions were removed, which caused an absolute error of only 0.003.

However, unlike other previously reported problems, decreasing the tolerance, it is not observed a proportional decrease in the relative error. This is due to the fact that the largest relative errors are concentrated in region R_4. This region has an average scalar flux significantly lower than the other regions, being in the order of 10^{-5}. Thus, any numerical fluctuation, no matter how small, causes fluctuations in the average scalar flux of this region.

Table 5.20: Computational time, relative error and number of removed subregions for different tolerances and number of subregions - Problem 6.

tol		$N_R = 1$	$N_R = 2$	$N_R = 5$	$N_R = 10$
	error	0	0	0	0
$tol = 0$	time (s)	38.76	129.15	1603.21	38888.88
	removed	0	0	0	0
	error	5.4719e-1	9.1996e-1	9.9564e-1	9.9975e-1
$tol = 10^{-1}$	time (s)	39.90	20.74	27.67	591.61
	removed	3436	61540	2494260	58857814
	error	5.4367e-1	7.8286e-1	9.4443e-1	9.7312e-1
$tol = 10^{-2}$	time (s)	41.01	24.37	45.54	947.56
	removed	3340	58796	2418560	57397238
	error	5.4367e-1	7.8286e-1	9.4443e-1	8.0983e-1
$tol = 10^{-3}$	time (s)	41.57	21.16	43.04	1795.10
	removed	3340	58796	2418560	55432032
	error	5.2463e-1	5.2744e-1	5.5608e-1	5.9969e-1
$tol = 10^{-4}$	time (s)	45.54	30.28	99.08	3292.73
	removed	2820	52448	2221740	53115286
	error	2.1089e-3	8.8195e-2	9.0731e-2	1.4830e-1
$tol = 10^{-5}$	time (s)	47.51	34.19	140.77	4546.11
	removed	2472	49084	2084932	50266878

Since using smaller tolerances, such as 10^{-2} and 10^{-3}, presents smaller errors, but is not proportional to the computational time used, which increases, almost doubling between each tolerance used. We consider here that the best configuration for this scenario is to use a tolerance of 10^{-1}.

Figure 5.6 provides insight into the distribution of scalar flux across the domain.

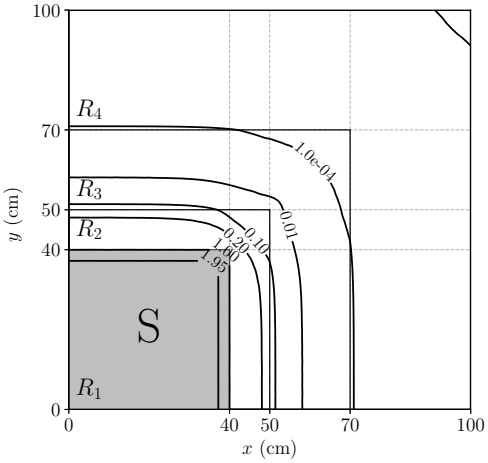

Figure 5.6: Contour lines of the scalar flux for Problem 6.

Note that the scalar flux is close to 2 for almost the entire region R_1, a region that has the largest macroscopic scattering cross section, $\sigma_s = 0.5$ cm^{-1}, and the internal source. As well as the flux decreases as it moves away from the source, which is expected physically. Furthermore, the amount of particles in the region R_4 is less than the order of 10^{-4}. Therefore, as mentioned, calculations in that region tend to suffer strong impacts from imprecise calculations in other regions, since we work with numbers on the order of 10^{-6}.

6 FINAL CONSIDERATIONS

In this study, we employed the integral formulation of the neutron transport equation, solving it through the Nyström method complemented by a singularity subtraction strategy. It was also combined with several numerical techniques, including subregioning and clipping technique, as a way to divide a problem into pieces, and remove unnecessary data, and reduce processing time. This approach was applied to six varied problems in X-Y geometry.

It was observed that for smaller areas, we could get accurate results quickly and with a small time cost. But, as the size of the domain increases, it becomes harder to get accurate results without spending more computational time and resources. Using the clipping technique was key. It gave us results just as precise as those from smaller areas but much faster.

Therefore, this study shows that mixing well-known methods with numerical techniques is crucial. This combination helps us get fast accurate results, matching what's already known and doing it efficiently. This combination highlights how we can improve both the speed and accuracy of solving complex problems like neutron transport problems by bringing together traditional methods and new ideas.

6.1 Perspectives

As presented in this work, and in the works of Azevedo *et al.* [13], Bublitz *et al.* [30] and Sauter *et al.* [89], the Nyström method combined with the singularity-removal technique has been used to solve neutron transport problems in the most varied conditions and geometries.

Despite the good results presented here, it is believed that more accurate results can be generated at an even lower computational cost. Mainly for

problems with larger domains, which are more complicated to produce accurate results and have a high computational cost.

In problems with large domains, 10 cm, 30 cm, and 100 cm, it was observed that the calculation of the terms of the Neumann series has been notably time-consuming. Therefore, exploring alternative iterative methods for solving the linear system, or using direct methods, could offer equally accurate outcomes more efficiently.

Furthermore, new problems can be addressed, such as problems with four reflecting boundary conditions and problems with different conditions of heterogeneity and isotropy.

REFERENCES

[1] Adams, M. L., and Larsen, E. W. Fast iterative methods for discrete-ordinates particle transport calculations. *Progress in nuclear energy 40*, 1 (2002), 3–159.

[2] Altaç, Z. Integrals Involving Bickley and Bessel Functions in Radiative Transfer, and Generalized Exponential Integral Functions. *Journal of heat transfer 118*, 3 (1996), 789–792.

[3] Altaç, Z., and Spinrad, B. I. The SK_N method i: A high-order transport approximation to neutron transport problems. *Nuclear Science and Engineering 106*, 4 (1990), 471–479.

[4] Altaç, Z., and Tekkalmaz, M. The SK_N approximation for solving radiation transport problems in absorbing, emitting, and scattering rectangular geometries. *Journal of Quantitative Spectroscopy and Radiative Transfer 73*, 2-5 (2002), 219–230.

[5] Altaç, Z., and Tekkalmaz, M. The synthetic kernel SK_N method applied to thermal radiative transfer in absorbing, emitting, and isotropically scattering homogeneous and inhomogeneous solid spherical medium. *J. Heat Transfer 125*, 4 (2003), 739–746.

[6] Altaç, Z., and Tekkalmaz, M. Benchmark solutions of radiative transfer equation for three-dimensional rectangular homogeneous media. *Journal of Quantitative Spectroscopy and Radiative Transfer 109*, 4 (2008), 587–607.

[7] Altaç, Z., and Tekkalmaz, M. Exact solution of radiative transfer equation for three-dimensional rectangular, linearly scattering medium. *Journal of Thermophysics and Heat Transfer 25* (04 2011), 228–238.

[8] Altaç, Z., and Tekkalmaz, M. Nodal synthetic kernel N-SK_N method for solving neutron transport equation in one- and two-dimensional X-Y geometries. *Annals of Nuclear Energy 64* (2014), 320–332.

[9] Altaç, Z., and Tekkalmaz, M. Radiative transfer in absorbing, emitting and isotropically scattering segregated two-layered, 3d rectangular enclosures. *Journal of Quantitative Spectroscopy and Radiative Transfer 133* (2014), 570–578.

[10] Altaç, Z. *The SK_N approximation: a new method for solving integral transport equations*. PhD thesis, Iowa State University, 1989.

[11] Altaç, Z., and Sert, Z. Application of alternative synthetic kernel approximation to radiative transfer in regular and irregular two-dimensional media. *Journal of Quantitative Spectroscopy and Radiative Transfer 187* (2017), 293 – 309.

[12] Anli, F., and Güngör, S. A spectral nodal method for one-group x, y, z-cartesian geometry discrete ordinates problems. *Annals of Nuclear Energy 23*, 8 (1996), 669–680.

[13] Azevedo, F. S., Sauter, E., Konzen, P. H. A., Thompson, M., and Barichello, L. B. Integral formulation and numerical simulations for the neutron transport equation in x-y geometry. *Annals of Nuclear Energy 112* (2018), 735–747.

[14] Azevedo, F. S., Thompson, M., Sauter, E., and Vilhena, M. T. Existence theory for a one-dimensional problem arising from the boundary layer analysis of radiative flows. *Progress in Nuclear Energy 53*, 8 (2011), 1105–1113.

[15] Azmy, Y. Comparison of three approximations to the linear-linear nodal transport method in weighted diamond-difference form. *Nuclear Science and Engineering 100*, 3 (1988), 190–200.

[16] Azmy, Y., and Sartori, E. *Nuclear computational science: a century in review*. Springer, 2010.

[17] Azmy, Y. Y. Multidimensional linear-linear nodal transport methods in weighted diamond difference form. Tech. rep., Oak Ridge National Lab., 1987.

[18] Badruzzaman, A. An efficient algorithm for nodal-transport solutions in multidimensional geometry. *Nuclear Science and Engineering 89*, 3 (1985), 281–290.

[19] Barichello, L. B., Cabrera, L. d. C., and Prolo Filho, J. F. An analytical approach for a nodal scheme of two-dimensional neutron transport problems. *Annals of Nuclear Energy 38*, 6 (2011), 1310–1317.

[20] Barichello, L. B., da Cunha, R. D., Picoloto, C. B., and Tres, A. An analytical approach for a nodal formulation of a two-dimensional fixed-source neutron transport problem in heterogeneous medium. *Kerntechnik 80*, 2 (2015), 167–173.

[21] Barichello, L. B., Picoloto, C. B., and da Cunha, R. D. The ADO-nodal method for solving two-dimensional discrete ordinates transport problems. *Annals of Nuclear Energy 108* (2017), 376–385.

[22] Barichello, L. B., and Siewert, C. E. A discrete-ordinates solution for a non-grey model with complete frequency redistribution. *Journal of Quantitative Spectroscopy and Radiative Transfer 62*, 6 (1999), 665–675.

[23] Barichello, L. B., Tres, A., Picoloto, C. B., and Azmy, Y. Y. Recent Studies on the Asymptotic Convergence of the Spatial Discretiza-

tion for Two-Dimensional Discrete Ordinates Solutions. *Journal of Computational and Theoretical Transport 45*, 4 (2016), 299–313.

[24] Bell, G. I., and Glasstone, S. Nuclear reactor theory. Tech. rep., US Atomic Energy Commission, Washington, DC (United States), 1970.

[25] Bertoline, G., Wiebe, E., Hartman, N., and Ross, W. *Fundamentals of Graphics Communication*, 6 ed. McGraw-Hill, 2010.

[26] Bickley, W. G. XXIV. Some solutions of the problem of forced convection. *The London, Edinburgh, and Dublin Philosophical Magazine and Journal of Science 20*, 132 (1935), 322–343.

[27] Bickley, W. G., and Nayler, J. XXV. A short table of the functions $\mathrm{Ki}_N(x)$, from n=1 to n=16. *The London, Edinburgh, and Dublin Philosophical Magazine and Journal of Science 20*, 132 (1935), 343–347.

[28] Boltzmann, L. Weitere studien uber warmegleichgewicht unter gasmolekulen (h-theorem). *Sitzungberichte der K. Wiener Academie 64* (1872), 275.

[29] Bublitz, C., de Azevedo, F. S., and Sauter, E. Nyström method applied to the transport equation in an axisymmetric cylinder. *Annals of Nuclear Energy 148* (2020), 107701.

[30] Bublitz, C., Lorensi, G. A., de Azevedo, F. S., and Sauter, E. Numerical results for radiative heat transfer in finite cylindrical medium with isotropic scattering. *Journal of Quantitative Spectroscopy and Radiative Transfer 280* (2022), 108087.

[31] Cacuci, D. G. *Handbook of Nuclear Engineering: Vol. 1: Nuclear Engineering Fundamentals*. Springer Science & Business Media, 2010.

[32] Carlson, B. G. Solution of the transport equation by sn approximations. Tech. rep., Los Alamos Scientific Lab., N. Mex., 1955.

[33] Chai, J. C., Lee, H. S., and Patankar, S. V. Ray effect and false scattering in the discrete ordinates method. *Numerical Heat Transfer, Part B Fundamentals 24*, 4 (1993), 373–389.

[34] Chen, X., and Sutton, W. Radiative transfer in finite cylindrical media using transformed integral equations. *Journal of Quantitative Spectroscopy and Radiative Transfer 77*, 3 (2003), 233–271.

[35] Courant, R., and Hilbert, D. *Methods of mathematical physics: partial differential equations*. John Wiley & Sons, 2008.

[36] Cox, A., Harris, S., Kyprianou, A., and Wang, M. Monte-carlo methods for the neutron transport equation. *SIAM/ASA Journal on Uncertainty Quantification* (Jan. 2022).

[37] Cromianski, S. R. *Um estudo sobre equações auxiliares em formulações nodais para solução da equação de transporte de nêutrons bidimensionais*. PhD thesis, PPGMAp-UFRGS, 2016.

[38] Cromianski, S. R., Rui, K., and Barichello, L. B. A study on boundary fluxes approximation in explicit nodal formulations for the solution of the two-dimensional neutron transport equation. *Progress in Nuclear Energy 110* (2019), 354–363.

[39] Dagnino, C., and Rabinowitz, P. Product integration of singular integrands using quasi-interpolatory splines. *Computers & Mathematics with Applications 33*, 1-2 (1997), 59–67.

[40] Dalmolin, D., De Azevedo, F. S., and Sauter, E. Nyström method in transport equation. In *Proceeding of INAC 2017 - Internation Nuclear Atlantic Conference, Rio de Janeiro, Brazil* (2017).

[41] De Abreu, M. P. Numerical methods for the generation of the spectrum of the multigroup slab-geometry discrete ordinates operator in neutron transport theory. *Annals of Nuclear Energy 29*, 15 (2002), 1837–1853.

[42] de Mello, J. A. M., and Barros, R. C. An exponential spectral nodal method for one-speed x, y-geometry deep penetration discrete ordinates problems. *Annals of Nuclear energy 29*, 15 (2002), 1855–1869.

[43] Delves, L. M., and Mohamed, J. L. *Computational Methods for Integral Equations*. Cambridge University Press, 1985.

[44] Domínguez, D. S., and Barros, R. C. The spectral green's function linear-nodal method for one-speed x,y-geometry discrete ordinates deep penetration problems. *Annals of Nuclear Energy 34*, 12 (2007), 958 – 966.

[45] DÖNER, N., and Altaç, Z. Solution of the radiative transfer equation using the synthetic kernel SK_N method in inhomogeneous participating and anisotropiclly scattering one dimensional cylindrical medium. *2nd International Conference on Thermal Engineering Theory and Applications* (2006).

[46] Döner, N., and Altaç, Z. Solution of the radiative transfer problems in two-dimensional participating cylindrical medium with isotropic scattering using the SK_N approximation. *2nd International Conference on Thermal Engineering Theory and Applications* (June 2006).

[47] Dorn, O., and Prieto, K. From data to images: A shape based approach for fluorescence tomography. In *Science: Image In Action*. World Scientific, 2011, pp. 255–266.

[48] Duderstadt, J. J., and Martin, W. R. *Transport theory*. John Wiley & Sons, 1979.

[49] Eberhard, G., Kohlschütter, A., and Ludendorff, H. *Handbuch der astrophysik*, vol. 3 of *Handbuch der astrophysik*. J. Springer, 1930.

[50] Franco, N. M. B. *Cálculo Numérico*. Pearson Hall, São Paulo, 2006.

[51] Ganapol, B. D. Analytical benchmarks for nuclear engineering applications. *Case Studies in Neutron Transport Theory. Organisation for Economic Co-operation and Development* (2008).

[52] Garcia, R. A review of the facile (F_N) method in particle transport theory. *Transport Theory and Statistical Physics 14*, 4 (1985), 391–435.

[53] Garcia, R., and Siewert, C. A multiregion calculation in the theory of neutron diffusion. *Nuclear Science and Engineering 76*, 1 (1980), 53–56.

[54] GNU Project. *GNU Scientific Library*.

[55] Golub, G., and Van Loan, C. *Matrix Computations*, 4 ed. JHU Press, 2013.

[56] Grandjean, P., and Siewert, C. The F_N method in neutron-transport theory. part ii: applications and numerical results. *Nuclear Science and Engineering 69*, 2 (1979), 161–168.

[57] Hauser, E. B., Pazos, R. P., Vilhena, M. T. d., and Barros, R. C. d. Solution and study of nodal neutron transport equation applying the LTS_N- diagexp method. In *Proceedings of the 18 ICTT: International conference on transport theory,* (Brazil, 2003), p. 355.

[58] Hou, M. F., and Wu, C. Y. Integral equation method applied to radiative transfer in a 2-D absorbing-scattering refractive medium. *International Communications in Heat and Mass Transfer 43* (2013), 63–68.

[59] Hsu, P. f., Tan, Z., and Howell, J. R. Radiative transfer by the YIX method in nonhomogeneous, scattering, and nongray media. *Journal of thermophysics and heat transfer 7*, 3 (1993), 487–495.

[60] Hu, Z. M., and Li, B. W. Benchmark solutions of radiative integral transfer equations for three-dimensional emitting–absorbing and scattering media bounded by gray walls. *Journal of Quantitative Spectroscopy and Radiative Transfer 113*, 6 (2012), 405–424.

[61] Johnson, S. G. Multi-dimensional adaptive integration in C: The Cubature package, 2005.

[62] Kanschat, G. A robust finite element discretization for radiative transfer problems with scattering. *East-West J. Numer. Math 6* (1998), 265 – 272.

[63] Lamarsh, J. R. Introduction to nuclear reactor theory. *Goldstein Herbert. Toi* (1966).

[64] Larsen, E. W., Thömmes, G., Klar, A., Seaïd, M., and Götz, T. Simplified P_N Approximations to the Equations of Radiative Heat Transfer and Applications. *Journal of Computational Physics 183*, 2 (2002), 652–675.

[65] Lathrop, K. D. Ray effects in discrete ordinates equations. *Nuclear Science and Engineering 32*, 3 (1968), 357–369.

[66] Lathrop, K. D. Remedies for ray effects. *Nuclear Science and Engineering 45*, 3 (1971), 255–268.

[67] Lawrence, R. D. Progress in nodal methods for the solution of the neutron diffusion and transport equations. *Progress in Nuclear Energy 17*, 3 (1986), 271 – 301.

[68] Lazzari, L. *Simulação do problema de transporte em domínio não homogêneo com espalhamento anisotrópico*. PhD thesis, PPGMAp-UFRGS, 2021.

[69] Lazzari, L., Sauter, E., and De Azevedo, F. S. Simulation for non-homogeneous transport equation by nyström method. *Brazilian Journal of Radiation Sciences 8*, 3A (2020).

[70] Lewis, E. E., and Miller, W. *Computational methods of neutron transport*. Wiley-Interscience, New York, 1984.

[71] Loyalka, S. K. A Numerical Method for Solving Integral Equations of Neutron Transport. *Nucl. Sci. Eng. 56*, 3 (1975), 317–319.

[72] Loyalka, S. K., and Naz, S. One speed black sphere problem: Some benchmark results. *Annals of Nuclear Energy 35*, 9 (2008), 1774–1778.

[73] Loyalka, S. K., and Tsai, R. W. A Numerical Method for Solving Integral Equations of Neutron Transport-II. *Nuclear Science and Engineering 58*, 2 (1975), 193–202.

[74] Maiorino, J. R. A equação de transporte de boltzmann e sua importância para a física dos reatores nucleares. *Revista Brasileira de Ensino de Física 29*, 1 (2007), 1–2.

[75] Mattson, T., and Meadows, L. A "hands-on" introduction to OpenMP. *Intel Corporation* (2014).

[76] Miralles, J. A., Van Riper, K. A., and Lattimer, J. M. The boltzmann equation in general relativistic rotating systems-cooling of rotating neutron stars. *The Astrophysical Journal 407* (1993), 687–698.

[77] Modest, M. F. *Radiative heat transfer*, 2 ed. Academic Press, San Diego, 2003.

[78] Naz, S., and Loyalka, S. K. One speed criticality problems for a bare slab and sphere: Some benchmark results – II. *Annals of Nuclear Energy 35*, 12 (2008), 2426–2431.

[79] Nunes, C. E. A., and Barros, R. C. Aplicativo computacional para cálculos de blindagem com modelo de transporte S_N unidimensional e monoenergético. In *Proceeding of INAC 2009 International Nuclear Atlantic Conference, Rio de Janeiro, Brazil* (2009).

[80] Nyström, E. J. Über Die Praktische Auflösung von Integralgleichungen mit Anwendungen auf Randwertaufgaben. *Acta Mathematica 54*, 1 (1930), 185–204.

[81] Olbrant, E., Larsen, E. W., Frank, M., and Seibold, B. Asymptotic derivation and numerical investigation of time-dependent simplified P_N equations. *Journal of Computational Physics 238* (2013), 315–336.

[82] Picoloto, C. B., Tres, A., da Cunha, R. D., and Barichello, L. B. Closed-form solutions for nodal formulations of two dimensional transport problems in heterogeneous media. *Annals of Nuclear Energy 86* (2015), 65–71.

[83] Pomraning, G. C. *Linear kinetic theory and particle transport in stochastic mixtures*, vol. 7. World Scientific, 1991.

[84] Press, W. H., Flannery, B. P., Teukolsky, S. A., Vetterling, W. T., et al. *Numerical recipes*. Cambridge university press Cambridge, 1989.

[85] Prolo Filho, J. F., and Rodrigues, M. P. A closed form solution for a one-dimensional multi-layered neutron transport problem by analytical discrete ordinates method. In *Defect and Diffusion Forum* (2017), vol. 372, Trans Tech Publ, pp. 50–59.

[86] Ramankutty, R., and Crosbie, A. L. Modified discrete-ordinates solution of radiative transfer in three-dimensional rectangular enclosures. *Journal of Quantitative Spectroscopy and Radiative Transfer 60*, 1 (1998), 103–134.

[87] Rodriguez, B. D. d. A., Vilhena, M., Hoff, G., and Bodmann, B. E. J. A closed-form solution for the two-dimensional transport equation by the ltsn nodal method in the energy range of compton effect. *Annals of Nuclear Energy 38*, 1 (2011), 151–156.

[88] Sanchez, R., and Ganapol, B. D. Benchmark values for monoenergetic neutron transport in one-dimensional cylindrical geometry with linearly anisotropic scattering. *Nuclear Science and Engineering 84*, 1 (1983), 61–67.

[89] Sauter, E., de Azevedo, F., and Konzen, P. Nyström method applied to the transport equation in a semi-reflective rectangle. *Journal of Computational and Theoretical Transport* (2019), 520–541.

[90] Scheben, F. *Iterative Methods for Criticality Computations in Neutron Transport Theory*. PhD thesis, University of Bath, Claverton Down, 2011.

[91] Schulz, D. M. *Métodos de aceleração para a solução da equação de transporte*. PhD thesis, PPGMAp-UFRGS, 2018.

[92] Semendyayev, I. B. K., and Mühlig, G. M. H. *Handbook of Mathematics*. Springer, 1997.

[93] Siewert, C., and Benoist, P. The F_N method in neutron-transport theory. part i: Theory and applications. *Nuclear Science and Engineering 69*, 2 (1979), 156–160.

[94] Spinrad, B. I., and Altaç, Z. The SK_N method ii: Heterogeneous problems. *Nuclear Science and Engineering 106*, 4 (1990), 480–488.

[95] Steward, F., and Cannon, P. The calculation of radiative heat flux in a cylindrical furnace using the monte carlo method. *International Journal of Heat and Mass Transfer 14*, 2 (1971), 245–262.

[96] Tan, Z., and Howell, J. R. Combined radiation and natural convection in a two-dimensional participating square medium. *International Journal of Heat and Mass Transfer 34*, 3 (1991), 785–793.

[97] Tan, Z., Hsu, P., Wu, S., and Wu, C. The QM-YIX method and adaptive angular quadrature for ray effects mitigation. Tech. rep., Florida Inst. of Tech., Melbourne, FL (US), 1999.

[98] Tan, Z.-M., and Hsu, P.-F. Transient radiative transfer in three-dimensional homogeneous and non-homogeneous participating media. *Journal of Quantitative Spectroscopy and Radiative Transfer 73*, 2 (2002), 181–194. Third International Symposium on Radiative Transfer.

[99] Tekkalmaz, M., and Altac, Z. Solution of radiative transfer problems in participating, linearly anisotropically scattering hollow spherical medium with SK_N method. *J. of Thermal Science and Technology 27*, 1 (2007), 23–38.

[100] Tres, A., Picoloto, C. B., Filho, J. P., da Cunha, R. D., and Barichello, L. B. Explicit formulation of a nodal transport method for discrete ordinates calculations in two-dimensional fixed-source problems. *Kerntechnik 79*, 2 (2014), 155–162.

[101] Tsai, R. W., and Loyalka, S. K. Numerical method for solving integral equations of neutron transport: III. *Nuclear Science and Engineering 61* (1976), 536–540.

[102] Vargas, R., Segatto, C., and Vilhena, M. Solution of the radiative heat transfer equation with internal energy sources in a slab by the LTS_N

method. *Journal of Quantitative Spectroscopy and Radiative Transfer 105*, 1 (2007), 1–7.

[103] Werner, D. *Funktionalanalysis*. Springer-Verlag, 2006.

[104] Wu, M., Yin, B., Vosoughi, A., Studer, C., Cavallaro, J. R., and Dick, C. Approximate matrix inversion for high-throughput data detection in the large-scale mimo uplink. In *2013 IEEE international symposium on circuits and systems (ISCAS)* (2013), IEEE, pp. 2155–2158.

[105] Yosida, K. *Functional Analysis*, 6th ed. Springer-Verlag, Berlin, 1995.

[106] Zhu, A. *Transient methods for pin-resolved whole-core neutron transport*. PhD thesis, Doctoral thesis, The University of Michigan, 2016.